(12)

AFGL-TR-83-0167

THE EFFECTS OF NATURALLY-OCCURRING PROPAGATION DISTURBANCES ON DISCRETE FOCUSED ARRAYS

Charles L. Rino
Robert C. Livingston
Nancy B. Walker
Michael D. Cousins

SRI International
333 Ravenswood Avenue
Menlo Park, CA 94025

Final Report
January 1982 - December 1982

March 1983

Approved for public release; distribution unlimited

AIR FORCE GEOPHYSICS LABORATORY
AIR FORCE SYSTEMS COMMAND
UNITED STATES AIR FORCE
HANSCOM AFB, MASSACHUSETTS 01731

This report has been reviewed by the ESD Public Affairs Office (PA) and is releasable to the National Technical Information Service (NTIS).

This technical report has been reviewed and is approved for publication.

Herbert Whitney
HERBERT E. WHITNEY
Contract Manager

Herbert C. Carlson Jr.
HERBERT C. CARLSON, JR.
Branch Chief

FOR THE COMMANDER

Rita C. Sagalyn
RITA C. SAGALYN
Division Director

Qualified requestors may obtain additional copies from the Defense Technical Information Center. All others should apply to the National Technical Information Service.

If your address has changed, or if you wish to be removed from the mailing list, or if the addressee is no longer employed by your organization, please notify AFGL/DAA, Hanscom AFB, MA 01731. This will assist us in maintaining a current mailing list.

Do not return copies of this report unless contractual obligations or notices on a specific document requires that it be returned.

UNCLASSIFIED

SECURITY CLASSIFICATION OF THIS PAGE (When Data Entered)

REPORT DOCUMENTATION PAGE		READ INSTRUCTIONS BEFORE COMPLETING FORM
1. REPORT NUMBER AFGL-TR-83-0167	2. GOVT ACCESSION NO. A132645	3. RECIPIENT'S CATALOG NUMBER
4. TITLE (and Subtitle) THE EFFECTS OF NATURALLY-OCCURRING PROPAGATION DISTURBANCES ON DISCRETE FOCUSED ARRAYS		5. TYPE OF REPORT & PERIOD COVERED Final Report for Period January 1982-December 1982
		6. PERFORMING ORG. REPORT NUMBER SRI Project 4017
7. AUTHOR(s) Charles L. Rino, Robert C. Livingston, Nancy B. Walker, Michael D. Cousins		8. CONTRACT OR GRANT NUMBER(s) Sandia Contract 69-9606
9. PERFORMING ORGANIZATION NAME AND ADDRESS SRI International 333 Ravenswood Avenue Menlo Park, CA 94025		10. PROGRAM ELEMENT, PROJECT, TASK AREA & WORK UNIT NUMBERS 62101F 464304CE
11. CONTROLLING OFFICE NAME AND ADDRESS Air Force Geophysics Laboratory Hanscom AFB, Massachusetts 01731 Monitor/Herbert E. Whitney/PHY		12. REPORT DATE March 1983 13. NO. OF PAGES 74
		15. SECURITY CLASS. (of this report) UNCLASSIFIED
14. MONITORING AGENCY NAME & ADDRESS (if diff. from Controlling Office) Sandia National Laboratories P. O. Box 5800 Albuquerque, NM 87185		15a. DECLASSIFICATION/DOWNGRADING SCHEDULE N/A

16. DISTRIBUTION STATEMENT (of this report)

Approved for public release; distribution unlimited

17. DISTRIBUTION STATEMENT (of the abstract entered in Block 20, if different from report)

18. SUPPLEMENTARY NOTES

19. KEY WORDS (Continue on reverse side if necessary and identify by block number)

scintillation
radar
auroral zone
polar cap
phase screen

20. ABSTRACT (Continue on reverse side if necessary and identify by block number)

The disruptive effects of ionospheric irregularities on space-based surveillance radars is considered. Propagation theory is used to first describe the parameters critical to such systems and to incorporate ionospheric parameters into that model. This is done using the equivalent phase screen approach with a statistical model of the in situ irregularity structure. The primary limitation that scintillation places on radar performance is the loss of spatial coherence, i.e., the resolving power of the radar. This, in turn, depends critically upon the turbulence strength, anisotropy, and motion of kilometer-scale irregularities.

DD FORM 1 JAN 73 1473

EDITION OF 1 NOV 65 IS OBSOLETE

UNCLASSIFIED

SECURITY CLASSIFICATION OF THIS PAGE (When Data Entered)

19. KEY WORDS (Continued)

20 ABSTRACT (Continued)

Although a complete spatial and temporal morphology of high-latitude structure is not yet known, data are available for near worst case performance estimates. Spaced receiver scintillation data directly provide all of the parameters critical to the performance analysis. Samples of such data from the auroral zone and central polar cap are presented; they show that radars with moderate-sized apertures may suffer degradation at some latitudes and local times.

CONTENTS

ILLUSTRATIONS

TABLES

I EXECUTIVE SUMMARY

The disruptive effects of naturally occurring propagation disturbances on communication and navigation systems are well known. More recently, however, antenna aperture synthesis techniques are being considered seriously for space-based surveillance and ground-based space surveillance. The applications include both passive and adaptive schemes. We shall refer to such systems as Discrete Focused Arrays (DFA).

To support the planning and evaluation of these new systems, the Air Force Geophysics Laboratory (AFGL) has tasked its scintillation research program to address the impact of naturally occurring propagation disturbances on such systems. This report draws on many facets of ongoing scintillation research to identify the critical parameters for the problem and to review the recent data that have been obtained to quantitatively define these parameters.

The propagation theory is now sufficiently well understood that we can characterize the signal structure fairly accurately in terms of a statistical description of the in situ irregularity structure. The in situ spectral density function is a sufficient statistic. In fact, for most engineering and many scientific applications, the ionospheric disturbance can be replaced by an equivalent phase perturbation without loss of generality.

The DFA problem can be separated into two parts. First the propagation theory is applied to determine the disruptive effects in the specific systems of interest. We have used a model (prototype) that encompasses the essential characteristics of any specific system. The propagation effects depend functionally on a mathematical description of the irregularity spectral density function, the most important parameter being the perturbation strength.

Second, the conditions under which severe performance degradations actually occur must be determined. This is the most difficult task because

it demands a detailed knowledge of the irregularity structure and its spatial and temporal morphology. In the report we first describe the DFA model and review the relevant parts of the propagation theory. The degradation of DFA performance involves two aspects of the signal structure. The temporal variations of the signal caused by the scintillation mainly affect the sensitivity of the DFA. Fading, for example, reduces target detectability. Similarly, phase scintillation limits the useful coherent integration time.

The synthesized antenna beam is affected directly by the spatial coherence of the wave field. The critical parameter is the spatial coherence scale compared to the effective size of the synthesized aperture; however, the spatial coherence of the wave field depends strongly upon the anisotropy of the irregularities. Our calculations show that an L-band array of more than a few hundred meters extent can suffer significant performance degradation during the most intense disturbances.

On the other hand, the regions in which such high-latitude disturbances occur are highly localized in latitude. Static models tend to exaggerate the likelihood of severe disturbances at a single location, particularly when geometrical effects are included. Truly predictive, dynamic models will ultimately be needed. Because the DNA HILAT satellite, scheduled for launch in summer of 1983, is dedicated to this problem, we have emphasized the scintillation phenomena that are relevant to global modeling as well as the aspects that directly relate to DFA performance.

II INTRODUCTION

Distributed antenna systems in which fixed (nonsteerable) elements independently measure phase-coherent signals and transmit them to a central processor are being considered for both passive and active surveillance systems. The resolution of such distributed focused arrays (DFA) is limited by the beam width of the individual elements, because all elements must illuminate the focus point.

To obtain a simple lower bound on the achievable resolution, let L_e be the effective aperture size of an array element. The maximum element separation that can contribute to a focus at R can be approximated as

$$L_{max} \cong \frac{R\lambda}{L_e} \quad . \tag{1}$$

Similarly, the corresponding spatial resolution of the DFA is

$$\Delta R \cong \frac{R\lambda}{L_{max}} = L_e \quad . \tag{2}$$

An example of such a system is SEASAT [Jordan, 1980], which uses aperture synthesis with a satellite-borne radar. For the two-way path, ΔR is half the effective aperture. SEASAT can achieve a ΔR of better than 10 m with digital processing.

For distributed focused arrays whose focus is within or beyond the ionosphere, however, the harmful effects of propagation disturbances must be considered. The general nature of propagation effects on DFA performance is easily understood. Over a single path, the propagation effects multiply the complex signal and cause the familiar temporal, amplitude, and phase scintillation structure. However, because the time-of-arrival differences to the various DFA elements are always much smaller than the scale for temporal changes in the scintillation structure, only the spatial structure of the scintillation affects the focusing operation.

The array is focused by forming a weighted summation of the complex signals at each element. It follows that any scintillation-induced defocusing can be described by a convolution in the spatial wave-number (angle) domain. As noted above, the time-dependent signal variations do not affect beam formation, but they do limit target detectability. For example, fading reduces the average signal-to-noise ratio. Similarly, the temporal coherence of the signal limits the time interval for effective coherent integration [Rino et al., 1977].

To calculate DFA performance degradation, we have developed a general model that can accommodate any DFA configuration. Propagation effects are described on each path by using the Huygens-Fresnel integral. An equivalent phase-screen relates the initial disturbance to the in situ irregularity structure. The model is used to calculate the average distortion of the DFA beam. For this application, the phase structure function is a sufficient characterization of the average propagation disturbance. The critical parameters are the spatial correlation scale and the anisotropy of phase perturbation.

To verify the model, we have analyzed a large data base of spaced-receiver measurements. Spaced-receiver measurements are important because from single-point measurements, neither the anisotropy nor the spatial scale of the wave field can be determined unambiguously. In fact, there is a complicated interplay between the anisotropy of the scintillation diffraction and its apparent drift. Spaced-receiver measurements allow us to determine the anisotropy and true pattern drifts. Temporal correlation scales can then be converted to spatial scales and the effects on DFA performance accurately predicted.

In addition to the large body of spaced-receiver data that have been analyzed, during November 1980 we performed a series of measurements using two independent GPS receiver systems with antennas separated by $\sim$ 100 m along an east-west baseline. The GPS satellites are in 12-hr orbits. Several GPS satellites were visible at high elevation angles for many hours at Poker Flat, Alaska, where the measurements were made. Thus, we had the opportunity to search for scintillation source regions and verify the DFA model for a single pair of elements.

III A DISCRETE FOCUSED-ARRAY MODEL FOR EVALUATING PROPAGATION EFFECTS

The model described in this section was developed for space-based radar applications [Rino, 1982a]. We modeled an arbitrary configuration of noninteracting, omnidirectional elements. For purposes of analysis, it is convenient to think of the elements as radiators. The nth element emits the spherical wave

$$\frac{\exp\{-ikr_n\}}{r_n} \quad . \tag{3}$$

By reciprocity, the problem is invariant to a source-receiver interchange.

If the nth element is located by the vector $\Delta\vec{\ell}_n$, then

$$r_n = R\left[1 + |\delta\vec{\ell}_n|^2 - 2\delta\vec{\ell}_n \cdot \hat{a}_R(\theta, \phi)\right]^{\frac{1}{2}} \tag{4}$$

where

$$\delta\vec{\ell}_n = \frac{\Delta\vec{\ell}_n}{R} \quad , \tag{5}$$

$\vec{R}$ is the distance from the center of the reference coordinate system to the tip of $\vec{r}_n$, and $\hat{a}_R$ is a unit vector along $\vec{R}$. The angles (θ, ϕ) locate the direction of $\vec{R}$.

We shall assume that $|\delta\vec{\ell}_n| << 1$ for the most remote DFA elements. Then, the approximation

$$r_n \simeq R + \tfrac{1}{2}\frac{|\Delta\vec{\ell}_n|^2}{R} - \Delta\vec{\ell}_n \cdot \hat{a}_R(\theta, \phi) \tag{6}$$

can be used. The array is "focused" by multiplying each element by the complex weighting factor $A_n \exp\{i\Phi_n\}$. The DFA field distribution, E_R,

is computed by summing the contributions from each element. Thus,

$$E_R(\theta, \phi) = \frac{\exp\{-ikR\}}{R}$$

$$\times \sum_n A_n \exp\left\{-i\left[-\Phi_n + \tfrac{1}{2}k\frac{|\Delta\vec{\ell}_n|^2}{R} - k\Delta\vec{\ell}_n \cdot \hat{a}_R(\theta, \phi)\right]\right\} \quad (7)$$

The quadratic term depends upon (θ, ϕ) through R, but only weakly, and can be absorbed in Φ_n without loss of generality. We can also ignore the spherical reference wave and consider only the DFA voltage pattern

$$V_R(\theta, \phi) = \sum_n A_n \exp\left\{-i\left[\Delta\Phi_n - k\Delta\vec{\ell}_n \cdot \hat{a}_R(\theta, \phi)\right]\right\} . \quad (8)$$

The array is focused by chosing $\Delta\Phi_n$ to cancel the linear $\Delta\vec{\ell}_n$ term for some fixed direction (θ_p, ϕ_p). In that case, we can write Eq. (8) in a simpler form as

$$V_R(\Delta\vec{K}) = \sum_n A_n \exp\{i\Delta\vec{\ell}_n \cdot \Delta\vec{K}\} \quad (9)$$

where

$$\Delta\vec{K} = -k\,\hat{a}_R(\theta_p, \phi_p) - \hat{a}_R(\theta, \phi) . \quad (10)$$

Thus, the voltage pattern of a DFA can always be written in the form of a discrete Fourier transform.

To accommodate propagation effects, we consider a phase screen located at a distance H from the array elements as shown in Figure 1. The propagation disturbance on each path is completely characterized by the complex time-varying function $h_n(t)$. Under even the most disturbed conditions, however, the temporal variations of $h_n(t)$ are very slow (greater than tens of milliseconds) compared to propagation delays within the array (less than tens of nanoseconds). Thus, insofar as array focusing is concerned, temporal changes are completely negligible,

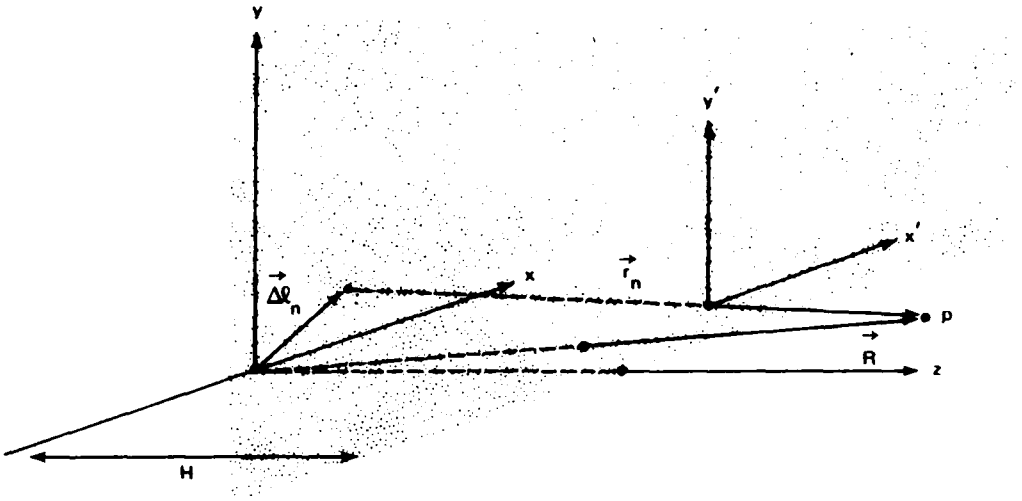

FIGURE 1 DNA COORDINATE SYSTEM FOR ANALYSIS OF DISTRIBUTED SYSTEM

and we can write

$$V_R(\vec{\Delta K}) = \sum_n A_n h_n \exp\{i\vec{\Delta\ell}_n \cdot \vec{\Delta K}\} \quad . \tag{11}$$

Even so, the temporal structure of the scintillation is ultimately of concern, because it limits the sensitivity (as opposed to spatial resolution) of the system. The fading and temporal coherence properties of scintillation signals are well known, however, and we shall concentrate mainly on the limitations to resolution. The fact that this partitioning can be performed greatly simplifies the problem.

To characterize h_n, we postulate a pure phase perturbation at H and then use the Huygens-Fresnel integral to calculate the evolution of the phase and amplitude structure. Using the phase-screen model is not unduly restrictive. Indeed, the average scintillation structure of the Wideband satellite data can be accurately reproduced by calculations based on the phase-screen model [Rino, 1982b].

The integral becomes unwieldy, however, if we fully accommodate the angle dependence of the ray path to each element. On the other hand,

under essentially the same conditions that Eq. (6) applies, we can ignore the angle dependence of the individual ray paths. If the array is focused on axis,

$$h_n = \iint \hat{u}(\vec{K}) \exp\left\{-i\vec{K}^2 \frac{r_e}{2k}\right\} \times \exp\{-i\vec{K} \cdot \vec{\rho}_n C\} \frac{d\vec{K}}{(2\pi)^2} \tag{12}$$

where

$$C = 1 - H/R \quad , \tag{13}$$

$$r_e = (1 - H/R)H \quad , \tag{14}$$

$$\vec{\rho}_n = \Delta\vec{\ell}_n \ (1 - H/R) \quad , \tag{15}$$

and $\hat{u}(\vec{K})$ is the Fourier transform of the phase perturbation in the plane at H. The general expression is given in Rino [1982a].

To accommodate the temporal structure of the scintillation, it is only necessary to replace $\vec{\Delta\ell}_n$ in Eq. (5) by $\vec{\Delta\ell}_n - \vec{v}_\perp t$, where $\vec{v}_\perp$ is the H-plane component of the apparent irregularity drift. The apparent drift accommodates antenna and target motion as well as the true irregularity drift. We assume that any change in the structure itself is negligible over time intervals of interest. With these assumptions, the model includes all potentially deleterious effects on DFA operation.

To make the model less abstract, we shall compute the average DFA power variation or gain pattern. For typical DFA applications, we attempt to direct the main beam and, in some applications, steer the side lobes to cancel out an interfering signal. In the absence of propagation effects, the power pattern is given by $|V_R(\vec{\Delta K})|^2$. As an example, for a uniformly-spaced linear DFA with $A_n = 1$,

$$|V_R(\vec{\Delta K})|^2 = \frac{\sin^2(N\vec{\Delta\ell}\vec{\Delta K}/2)}{\sin^2(\vec{\Delta\ell}\vec{\Delta K}/2)} \quad . \tag{16}$$

The beam width to first null is $\frac{\pi}{N\Delta\vec{\ell}}$, or in radians $\lambda/(2L)$. The main side lobes fall of as $\Delta\vec{K}^{-2}$.

Because the propagation disturbances are random, we consider the expectation value of $|V_R(\Delta\vec{K})|^2$. By direct computation from Eqs. (11) and (12),

$$\langle|V_R(\vec{\Delta K})|^2\rangle = \sum_n \sum_m \langle h_n h_m^*\rangle A_n A_m \exp\left\{i\Delta\vec{\rho}_{nm} \quad \Delta\vec{K}\right\} \tag{17}$$

where

$$\langle h_n h_m^*\rangle = \iint \Phi(\vec{K}) \exp\left\{-i\vec{K} \cdot \Delta\vec{\rho}_{nm} \; C\right\} \frac{d\vec{K}}{(2\pi)^2} \tag{18}$$

and $\Phi(\vec{K})$ is the spectral density function of the initial perturbation. In terms of the phase structure function,

$$\langle h_n h_m^*\rangle = \exp\left\{-\tfrac{1}{2} D_{\delta\varphi}(\Delta\vec{\rho}_{nm} C)\right\} \tag{19}$$

where

$$D_{\delta\phi}(\Delta\rho) = \langle[\delta\phi(\vec{\rho}) - \delta\phi(\vec{\rho}')]^2\rangle \quad . \tag{20}$$

It follows from Eq. (17) that the average distortion of the DFA beam is independent of the Fresnel radius. The only dependence on the propagation distance is contained in C [see Eq. (13)]. If H = R, then C = 0 and there is no distortion as we should expect. If R > > H, that is, the focus approaches infinity, then C = 1 and the propagation effects are maximized.

To carry the problem further, we identify the $\Delta\vec{\rho}$ contour such that $D_{\delta\phi}(\vec{\Delta\rho}) = 1$. As long as the DFA elements lie well within this contour, the DFA beam distortion will be small. To evaluate this contour explicitly, we use the approximation:

$$D_{\delta\phi}(\vec{\Delta\rho}) \cong C_{\delta\phi}^2 \, G \, f(\vec{\Delta\rho})^{\min[p-1,\, 2]} \tag{21}$$

where p is the phase power-law spectral index, and G is a geometrical factor that depends on the propagation angle relative to the magnetic field,

$$C_{\delta\phi}^2 = r_e^2 \lambda^2 \ell_p C_S F(p) \quad , \tag{22}$$

and

$$f^2(\Delta\rho) = \frac{C\Delta\rho_x^2 - B\,\Delta\rho_x\Delta\rho_y + A\Delta\rho_y^2}{AC - B^2/4} \quad . \tag{23}$$

In Eq. (22) r_e is the classical electron radius, λ is the wavelength, ℓ_p is the length of the propagation path within the disturbed region, C_S is the equivalent isotropic turbulence strength. The complete form of Eq. (22) and a definition of f(p) and the coefficients A, B, and C, which depend on the irregularity anisotropy and propagation geometry, can be found in Rino [1982b].

The important points to note here are that the average DFA beam distortion depends only on the perturbation strength, through $C_{\delta\phi}^2$ and the irregularity anisotropy through $f(\Delta\vec{\rho})$. The perturbation strength can be determined from phase scintillation measurements. The anisotropy can be determined unambiguously only by using spaced-receiving measurements [Rino and Livingston, 1982].

IV POKER FLAT GPS MEASUREMENTS

A. General Morphology

During November 1980, a series of measurements were made at Poker Flat, Alaska, using the GPS Navstar satellites as signal sources. The satellites are in 12-hour circular orbits and they transmit broadband (PRN) signals at two L-band frequencies, 1575.42 MHz (L1) and 1227.6 MHz (L2). With appropriate receiving equipment, it is possible to measure amplitude scintillation, the L1 to L2 differential phase scintillation, and the total electron content (TEC), as described in detail in Klobuchar [1981].

The 350-km ionospheric penetration points for the satellites visible through the local evening sector are plotted in Figure 2. The satellites progress from the north, and they are visible for more than two hours. The points of closest approach lie to the west of the Poker Flat observing station. The remaining passes, shown in Figure 3, provide more extended coverage but they occur well into the morning sector.

As discussed in Section II, two factors contribute to DFA beam distortion; namely, perturbation strength and irregularity anisotropy. The GPS observations were made to map the distribution of auroral-zone irregularities over large latitude and local-time sectors. Most other auroral-zone scintillation measurements have been made using either geosynchronous satellites, which are observed at low elevation angles, or low-orbiting satellites such as Wideband and TRANSIT. The former give good local time coverage, but poor localization of structure. Low-orbiting satellites give excellent latitudinal coverage, but only a coarse local time sampling. With several satellites in high-altitude orbits, the GPS constellation is ideally suited for nearly simultaneous local-time and latitudinal coverage.

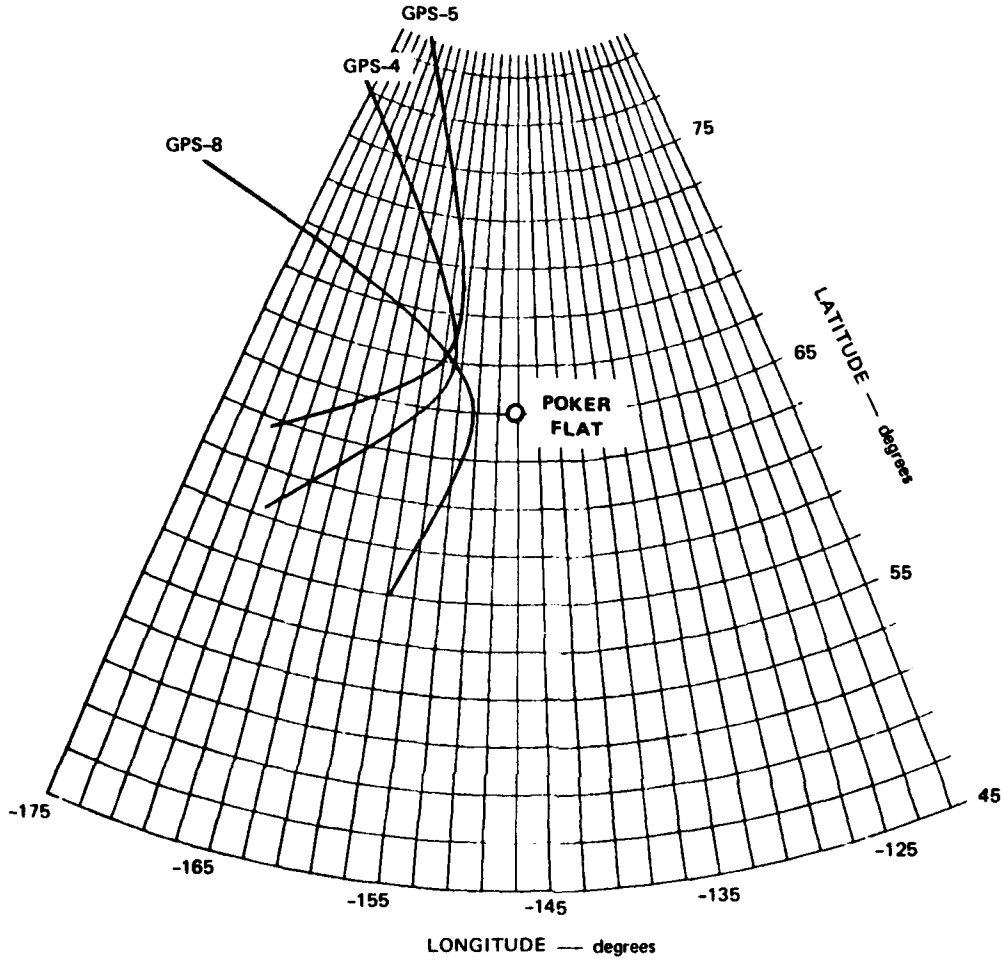

FIGURE 2 EVENING-SECTOR GPS PASSES

The most recent work on high-latitude scintillation morphology has been heavily influenced by data from the low-orbiting Wideband satellite [Fremouw and Lansinger, 1981; Basu et al., 1981]. In more than 40 percent of the nighttime passes recorded at Poker Flat, for example, a localized scintillation enhancement was observed at the point where the propagation path lay within the local L-shell. This has been attributed to a geometrical enhancement from sheetlike irregularities, although a localized source is also involved [see Rino and Vickrey, 1982, for a detailed discussion]. In any case, static (average) morphological models necessarily are heavily influenced by this geometrical factor.

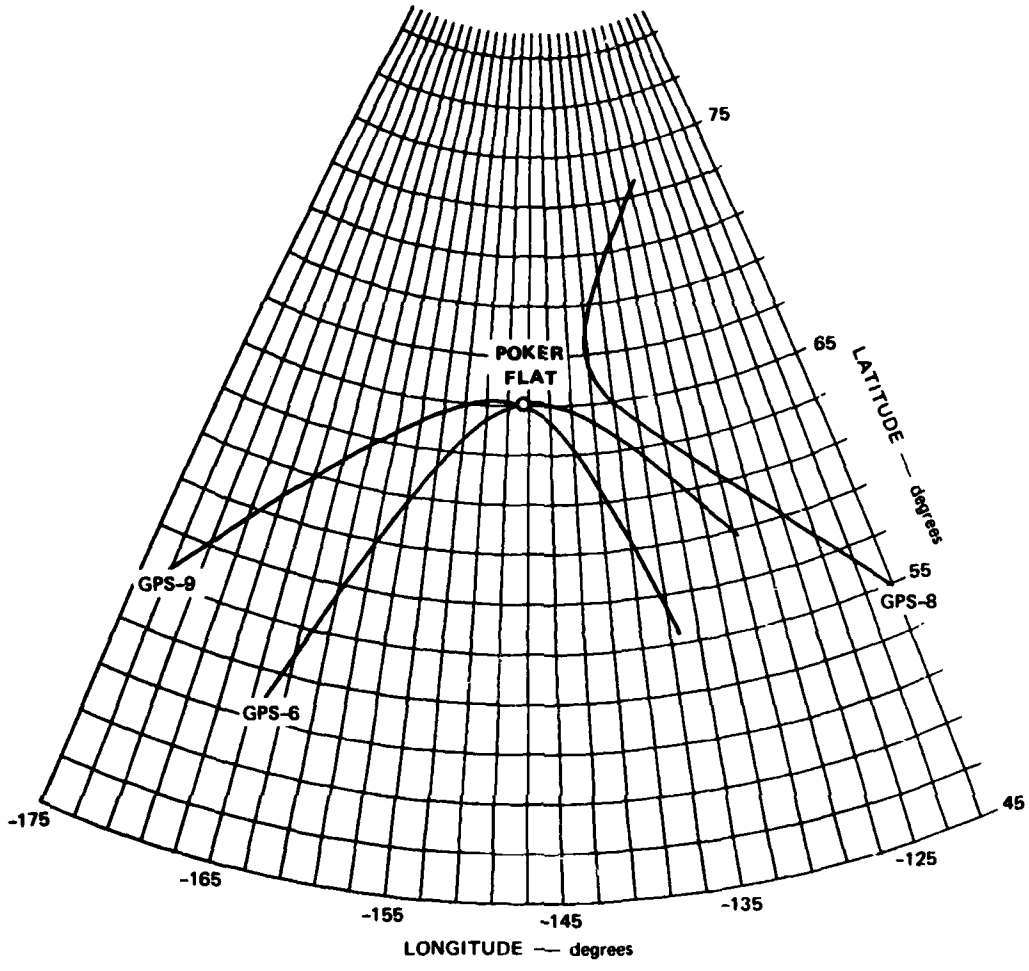

FIGURE 3 MORNING-SECTOR GPS PASSES

Because the GPS satellite moves very slowly through regions of higher geometrical enhancement, we expected a preponderance of enhanced scintillation events in these regions. A very different pattern was actually observed. We maintained a reasonably consistent schedule of operations for nine consecutive evenings. After that, the operation sequence was changed to accommodate dual-receiver measurements, which are described in Section III.

The measured L1 intensity scintillation for the first nine days is summarized in Figure 4. Local midnight at Poker Flat occurs at 10:00 UT. Superimposed on the data for Day 315 is the geometrical enhancement factor

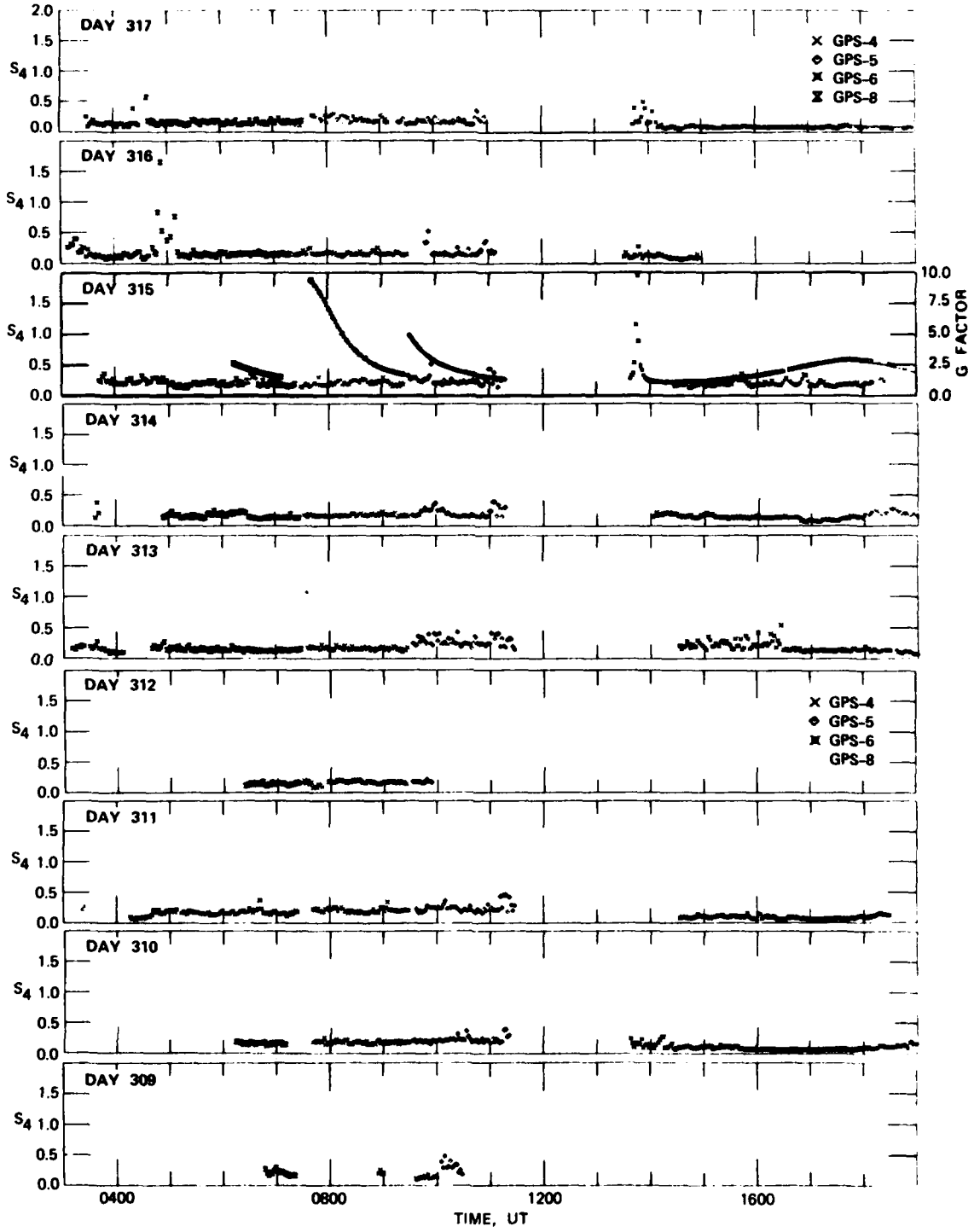

FIGURE 4 POKER FLAT GPS NOVEMBER 1981

for 10:10:1 sheetlike irregularities [Livingston et al., 1982]. The diurnal progression of the satellite passes is small enough that essentially the same pattern can be applied to any evening.

The most prominent sustained enhancement that can be associated with geometry occurs on the GPS 4 path just before 800 UT. A small, but consistent enhancement occurs on the GPS 5 path around 0930 UT. The dominant scintillation enhancement occurs near 1100 UT, however, where the geometrical enhancement factor is small. The persistence of this feature night after night clearly suggests that it is caused by a localized irregularity source region.

It is convenient to plot the data on an invariant magnetic latitude-local magnetic time plot. Figure 5 summarizes the first eight days of

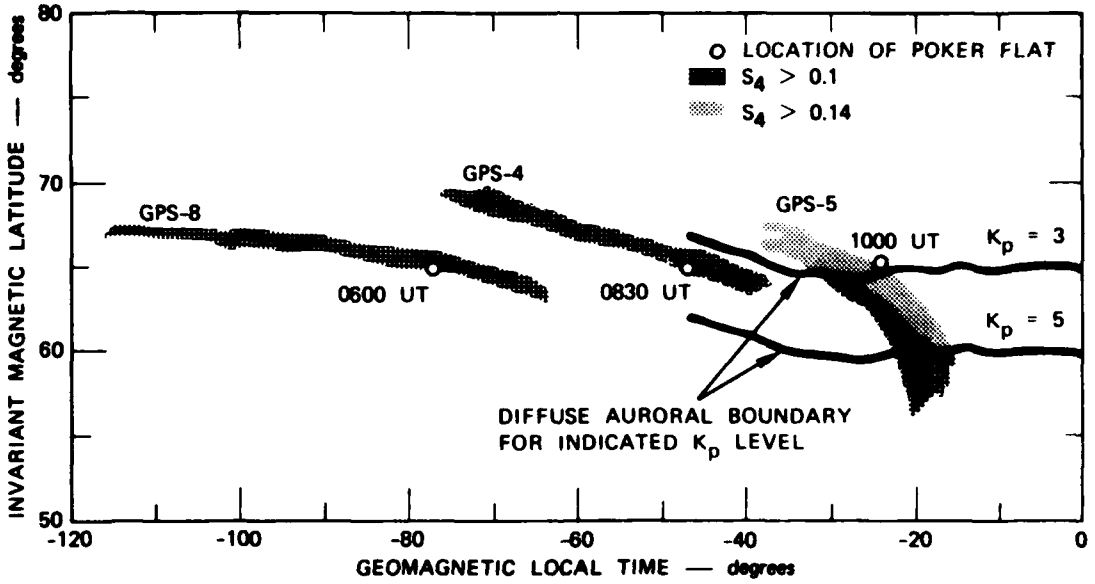

FIGURE 5 LOCATION OF SCINTILLATION ENHANCEMENTS

operation in this manner. The activity increases as we move equatorward and toward midnight; moreover, the region of the most prominent scintillation enhancement occurs near the expected location of the diffuse auroral boundary.

The Chatanika radar has provided unambiguous identification of localized scintillation enhancements that are most prominent when viewed along the local L-shell. This has been interpreted as a geometrical effect from sheetlike irregularities. On the other hand, the most recent Chatanika studies indicate that these structures are highly dynamic, possibly even transient factures. In addition, a much more stable "boundary blob" or wall of F-region ionization is located at the equatorward boundary of the diffuse auroral region.

The location of the persistent enhancement seen on GPS 5 is consistent with the expected location of the boundary blob as predicted by Tsunoda and Vickrey [1982]. These results are preliminary, but it is clear that accurate prediction of scintillation enhancements ultimately will require an understanding of the evolution and dynamics of these source regions.

The activity is summarized in Table 1, which lists the fractional number of data points with S_4 at L1 greater than 0.1, the maximum value of S_4 at L1 for the pass, and the College, Alaska 3-hour K index of magnetic activity. This comparatively small data set did not reveal a systematic dependence on the magnetic activity at the receiving station as was found in the Wideband satellite data [Rino and Matthews, 1980], probably because the 22,000-km height of the satellite generally places the ionospheric penetration point well removed from the vicinity of the station.

In summary then, over the eight-day period where a consistent GPS observing pattern was maintained, very similar occurrence patterns of enhanced scintillation were observed. A small enhancement was observed on GPS 4 before 0800 UT, which is consistent with the expected geometrical enhancement from sheetlike irregularities. The largest scintillation enhancements, however, were observed on GPS 8 after 1100 UT where the geometrical enhancement factor is minimized. Coincident Chatanika radar data have revealed a persistent enhanced F-region ionization "wall" that is possibly the source region of the dominant enhancement.

Table 1

GPS INTENSITY SCINTILLATION SUMMARY

Day	Satellite No.	$S_4 > 0.1$ (%)	Maximum S_4	Magnetic Activity (College K)
309	8	20	0.13	5
	4	20	0.14	5
310	8	41	0.13	1
	4	72	0.13	1, 3
	5	91	0.17	3
311	8	34	0.18	5
	4	72	0.14	5, 4
	5	94	0.15	4 (5 after midnight)
313	8	4	0.12	1, 3
	4	38	0.12	3
	5	83	0.26	3
314	8	7	0.13	2
	4	1	0.10	6 (isolated substorm)
	5	25	0.26	4
315	8	7	0.23	3
	4	34	0.13	3
	5	63	0.18	3 (8 after midnight)
316	8	1	0.10	6
	4	1	0.11	6, 5
	5	17	0.18	5
317	8	1	0.18	0
	5	3	0.15	1

B. Computation of Phase Turbulence Strength

We showed in Section I that the beam distortion in a DFA depends critically on the phase structure constant as defined by Eq. (22). The scintillation model that we have used extensively is based on a three-dimensional in situ spectrum of the form

$$\Phi_{\Delta N_e}(\vec{K}, K_z) = \frac{C_S}{\left[q_o^2 + q^2\right]^{\nu + \frac{1}{2}}} \qquad (24)$$

where q is a quadratic form on the vector elements k_x, k_y, and k_z. If Eq. (24) is integrated over all spatial wave numbers, the rms electron density can be computed as

$$\langle \Delta N_e^2 \rangle = C_S \, q_o^{-(2\nu - 2)} \frac{\Gamma(\nu - 1)}{8\pi 3/2 \, \Gamma(\nu + \frac{1}{2})} \quad . \tag{25}$$

Thus, if a value of q_o is specified, C_S and ΔN_e^2 are interchangeable. As a practical matter, the spatial homogeneity required for a meaningful spectral definition is generally violated before an outer-scale cutoff can be identified. Nonetheless, power-law segments such as

$$\Phi_{\Delta N_e} = C_S q^{-(2\nu + 1)} \qquad q_{min} \leq q \leq q_{max} \tag{26}$$

can be deduced from measurable one-dimensional spectra.

For example, an in situ probe measures a one-dimensional spectrum of the form

$$\Phi_{\Delta N_e}^{(1)}(q) = C_S^{(1)} \, q^{-p_1} \tag{27}$$

where

$$C_S^{(1)} = \frac{C_S \Gamma(\nu - \frac{1}{2})}{4\pi^2 \Gamma(\nu + \frac{1}{2})} \tag{28}$$

and

$$p_1 = 2\nu - 1 \quad . \tag{29}$$

The actual value of q depends on the scan rate and the scan direction. This relation was used by Livingston et al. (1981) to compare in situ AE-E satellite data with phase scintillation data from the Wideband satellite.

For phase scintillation data, we measure a temporal phase spectrum of the form

$$\varphi(f) = Tf^{-p} \tag{30}$$

where

$$T = C_p \, G \, \frac{\sqrt{\pi} \, \Gamma(\nu)}{(2\pi)^{2\nu + 1} \, \Gamma(\nu + \frac{1}{2})} \, v_{eff}^{2\nu - 1} \quad , \tag{31}$$

$$p = 2\nu \quad , \tag{32}$$

and

$$C_p = r_e^2 \, \lambda^2 \ell_p \, C_S \quad . \tag{33}$$

As discussed in Rino (1982b), Eq. (22) can be approximated by the simpler

$$C_{\delta\phi}^2 \cong \frac{C_p}{2\pi} (\nu^2 - 4.5\nu + 5.5) \qquad 1.0 < \nu < 2.0 \quad . \tag{34}$$

Hence, once C_p and ν are determined, $C_{\delta\phi}^2$ can be computed.

The major uncertainty in determining C_p from T is the effective scan velocity v_{eff}, which depends on both the irregularity anisotropy and the apparent irregularity drift. Because the auroral-zone field lines are nearly vertical, for rodlike irregularities v_{eff} is simply the magnitude of the component of the apparent drift velocity perpendicular to the line of sight. For sheetlike irregularities, however, the east-west component of the apparent velocity is reduced by the east-west enhancement factor. The apparent velocity itself results from the true irregularity drift and the motion of the ionospheric penetration induced by the signal source or receiver. For the GPS observations, the source motion is negligible because of the 12-hour orbits.

To illustrate the interplay between anisotropy and the temporal to spatial conversion factor v_{eff}, a plot of v_{eff} for a 100-mps westward drift is shown in Figure 6. The two sets of curves are for 5:1 rods and 5:5:1 sheets. For sheets, the temporal-to-spatial conversion factor is fairly uniform and the true drift is recovered directly. For rods, there is much more variation. With a single point measurement, there is no way to resolve such ambiguities.

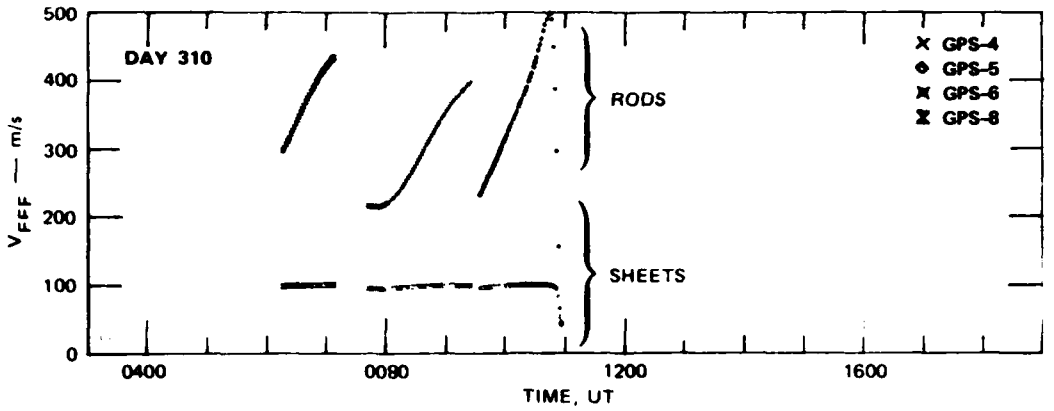

FIGURE 6 EFFECTIVE VELOCITY FOR TEMPORAL TO SPATIAL CONVERSION

To illustrate the general characteristics of the phase scintillation data, in Figure 7 we show the phase data for GPS 5 on Day 310, after a 300-s detrend filter was applied. Spectral analysis was then performed on 15-min overlapping segments. Two representative spectra are shown in Figure 7. It is important to note that the aggregate disturbance for the earlier spectrum is larger than for the second disturbance, even though the latter shows a larger peak-phase disturbance. Peak-to-peak phase excursions in excess of 20 radians are associated with all the moderately disturbed data segments. That fact alone, however, gives no useful information about disruptive system effects.

The spectral data have been smoothed and summarized by the power-law parameters T and p obtained from a log-linear least-squares fit over the temporal frequency range 0.01 to 0.05 Hz. On average, the spectral slopes are steeper than those measured using Wideband satellite data. This is very likely from temporal variations within the comparatively long (30-min) data segments. The GPS data show a systematic decrease in the spectral slope with increasing perturbation strength as has been consistently observed in the Wideband satellite data. This is illustrated in the p vs. $\log_{10}T$ plot shown in Figure 8, which summarizes the GPS 5 data for four evenings. The straight line was hand drawn. Similar plots for Wideband satellite data show the same trend, but displaced to a median value of ~ -2.5 rather than ~ -3.0.

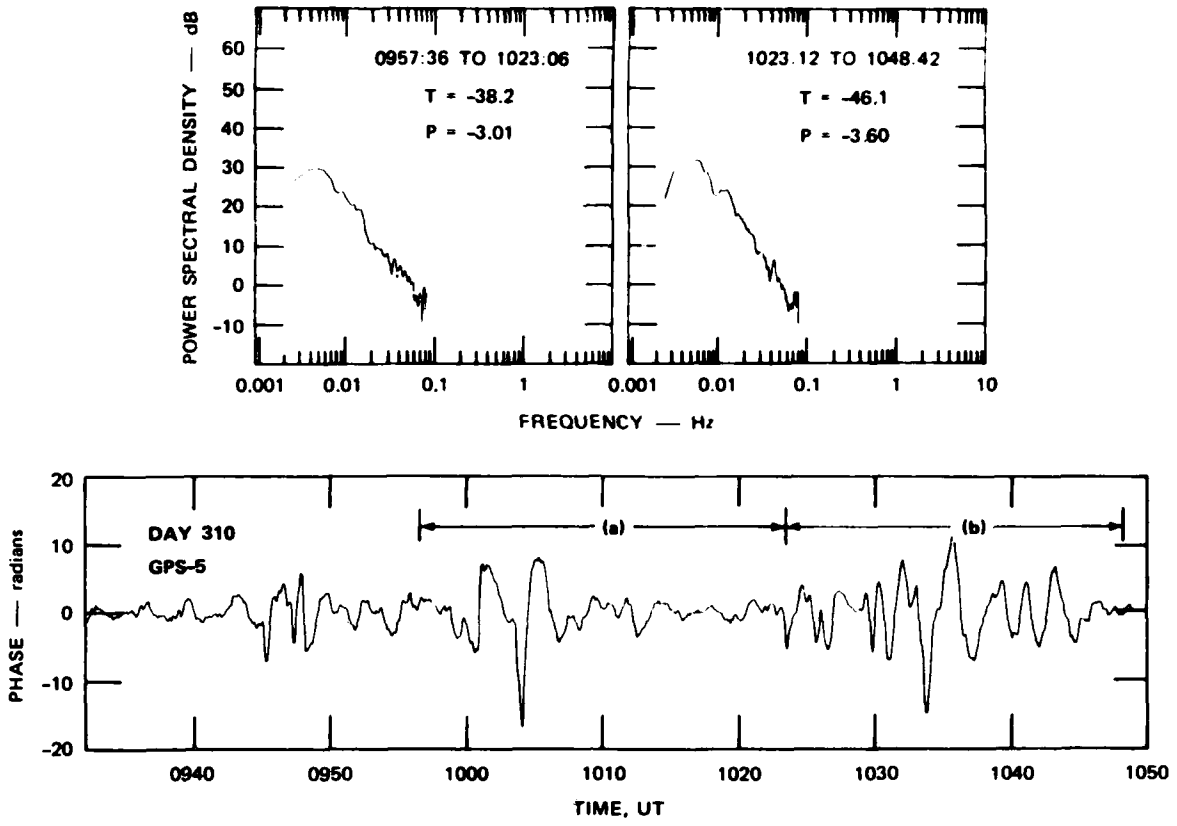

FIGURE 7 GPS PHASE SPECTRA (DAY 310)

For equatorial data there is a consistent $\sim$ 5:1 ratio between the effective scan velocities for the low-orbiting Wideband satellite and GPS. In the Wideband satellite phase scintillation data, the temporal frequencies that are least affected by diffraction generally correspond to scale sizes greater than one kilometer. Thus, the Wideband satellite equatorial phase data are heavily weighted toward the "intermediate-scale regime" where the slopes are shallow and vary systematically [Livingston et al., 1981]. The corresponding range of scale sizes for the GPS equatorial data possibly lies below one kilometer where the spectrum shows a distinctly different behavior [Rino et al., 1981].

In the auroral zone, the in situ drifts are substantially larger and more variable than the equatorial drifts. Thus, we do not have a sharp separation of the scale-size regimes sampled by Wideband and by

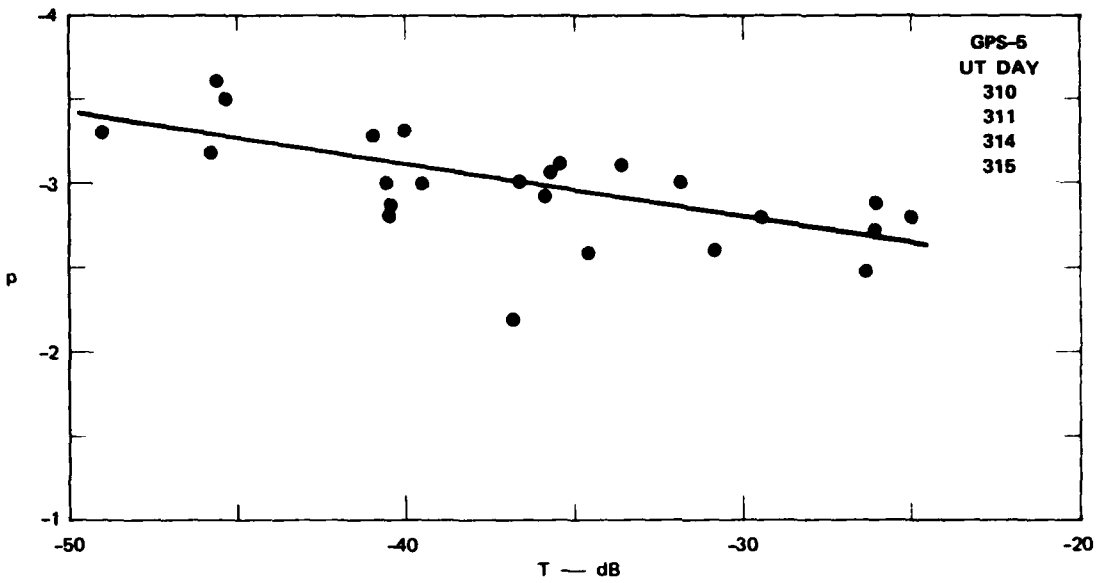

FIGURE 8 SPECTRAL INDEX VARIATION

GPS; moreover, because the auroral-zone is much richer in plasma source mechanisms, irregularity drivers and coupling regions, the spectral characteristics themselves are likely to be more varied.

C. Single Baseline Spaced-Receiver Measurements

To complete the analysis of DFA beam smearing, we need to know the anisotropy of the diffraction pattern. To resolve the anisotropy, unambiguously, multireceiver measurements are required [*Rino and Livingston*, 1982]. On the other hand, a single spaced-receiver measurement is the simplest DFA configuration that retains all the essential elements of the system. In the plane of the DFA, the correlation function of the field admits a representation of the form

$$R[\tilde{f}(\Delta\vec{\rho}' - \vec{v}'\,\delta t)] \tag{35}$$

where

$$\tilde{f}^2(\vec{\zeta}) = \left[C'\zeta_x^2 - B'\zeta_x\zeta_y + A'\zeta_y^2\right]/[A'C' - B'^2/4] \quad . \tag{36}$$

As discussed in Rino and Livingston [1982], the anisotropy of the signal intensity and the signal phase is essentially the same as the complex signal itself; however, because of the small perturbations levels at L band, we shall use only signal phase.

By operating two independent dual-frequency GPS receiver systems, we were able to make displaced-point measurements of the signal phase from a common source. Because the transmission time is modulated onto the data stream and because the pseudo-range delay differences are at most many tens of nanoseconds even without bias removal, the phase measurements can be coherently processed for phase comparisons. Indeed, this is the phase error that a 100-m linear DFA would encounter if it were "focused" on the GPS satellite. Because the error is random, the degree of phase decorrelation between the two receivers is the quantity of interest; call it $R_\phi(\Delta\vec{\rho})$.

We have shown, however, that the phase structure function, Eq. (20), is the quantity that characterizes the average DFA beam distortion. The formal interrelation is

$$D_{\delta\phi}(\Delta\vec{\rho}) = 2[R_\phi(0) - R_\phi(\Delta\vec{\rho})] \quad , \tag{37}$$

provided that diffraction effects in the signal phase are negligible. The effect of Eq. (37) is to suppress the contribution of large-scale structures. Treatments that proceed directly from $R_\phi(\Delta\vec{\rho})$ invariably extract these low frequency components [Elachi and Evans, 1977].

If a coordinate system with one axis along the receiver baseline is used, Eq. (35) can be rewritten as

$$R[(\ell_b - v_a\delta t)/\ell_c] \tag{38}$$

where ℓ_b is the baseline length, v_a is the apparent velocity, and ℓ_c is the apparent correlation scale. The problem with single baseline measurements is that ℓ_c and v_a are not simply related to the minimum spatial coherence scale and the effective or true pattern drifts.

Unfortunately, the data acquisition system (which was rapidly constructed just before the experiment) for the second receiver, did not perform well, and we obtained only a few coincident data sets during interesting scintillation events. These are summarized in Table 2. The first two columns list the maximum value of the cross-correlation function and its delay offset, respectively. The remaining columns summarize the phase spectral characteristics at the individual receivers. The fact that the spectral characteristics are identical to within the statistical accuracy of the measurements is a good indication that all the instrumental effects have been removed.

The actual phase records and the measured cross correlation functions for days 318 and 320 are shown in Figures 9 and 10, respectively. The data in Figure 9 were taken during active positive bay conditions as recorded on the College, Alaska magnetometer. For $\tau_a \sim 1$ and $\ell_b \sim 100$ m, v_a is approaching 1 km/s. Unlike the effective velocity for converting temporal scales to spatial scales (v_{eff}), the apparent pattern drift will always be larger than the true drift. Thus, large values of v_a are more indicative of enhanced correlation scales along the baseline that increases in the pattern drift. The τ_a values approaching 0.9, however, correspond to several hundred meter-per-second east-west drifts which are consistent with Chatanika radar drift measurements made under similar conditions.

The data shown in Figure 10 are more interesting in that they show an abrupt change in activity around 928 UT. An abrupt negative bay onset was observed on the College magnetometer just before 900 UT. Because the GPS 5 satellite was almost 10° to the west of Poker Flat, this event probably marks the passage of the westward expansion of the activity to the ionospheric penetration point. The eastward drift component ($v_a < 0$) of $\sim$ 600 mps is reasonable for an active eastward electrojet.

Thus the GPS dual-receiver measurements seem to produce credible measurements that can be exploited further. Insofar as DFA performance is concerned, for the perturbation levels experienced here, there was essentially no phase decorrelation on a 100-m baseline. It follows that small DFA systems operating at L band or higher would experience no significant beam degradation. This will be shown quantatively in Section 5 in which all the results are discussed and conclusions drawn.

Table 2

GPS SPACED-RECEIVER SUMMARY

Day	Times (UT)	Maximum Correlation	Delay (s)	T_1 (dB)	T_2 (dB)	P_1	P_2
318 (GPS-4)	0741 to 0807	0.93	0.12	- 44	- 45	- 2.6	- 2.7
	0754 to 0819	0.83	0.94	- 44	- 43	- 2.7	- 2.6
	0807 to 0832	0.92	0.80	- 42	- 48	- 2.5	- 2.8
319 (GPS-6)	1451 to 1517	0.94	- 0.13	- 33	- 32	- 2.2	- 2.1
	1503 to 1528	0.99	- 0.05	- 26	- 28	- 1.8	- 1.9
	1516 to 1541	0.99	- 0.02	- 32	--	- 2.3	---
320 (GPS-5)	0905 to 0930	0.99	0.01	- 55	- 60	- 3.6	- 3.9
	0912 to 0937	0.96	- 0.29	- 42	- 45	- 3.1	- 3.2

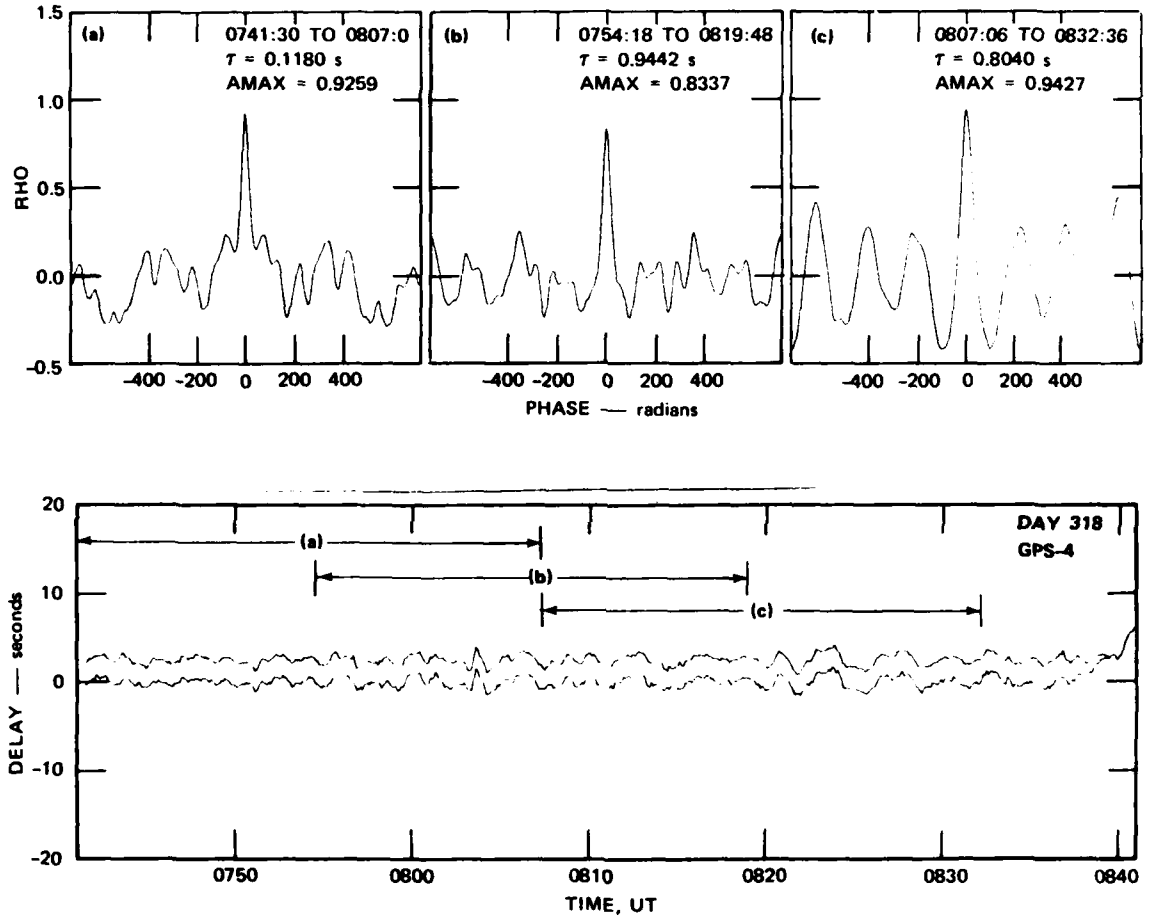

FIGURE 9 GPS SPACED-RECEIVER MEASUREMENTS (DAY 318)

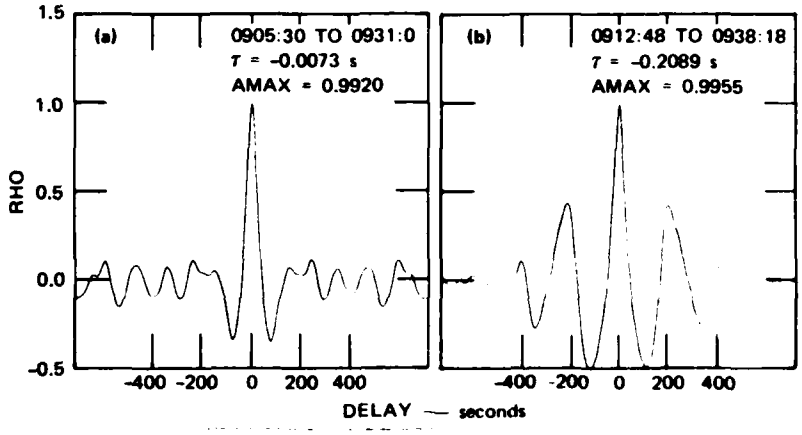

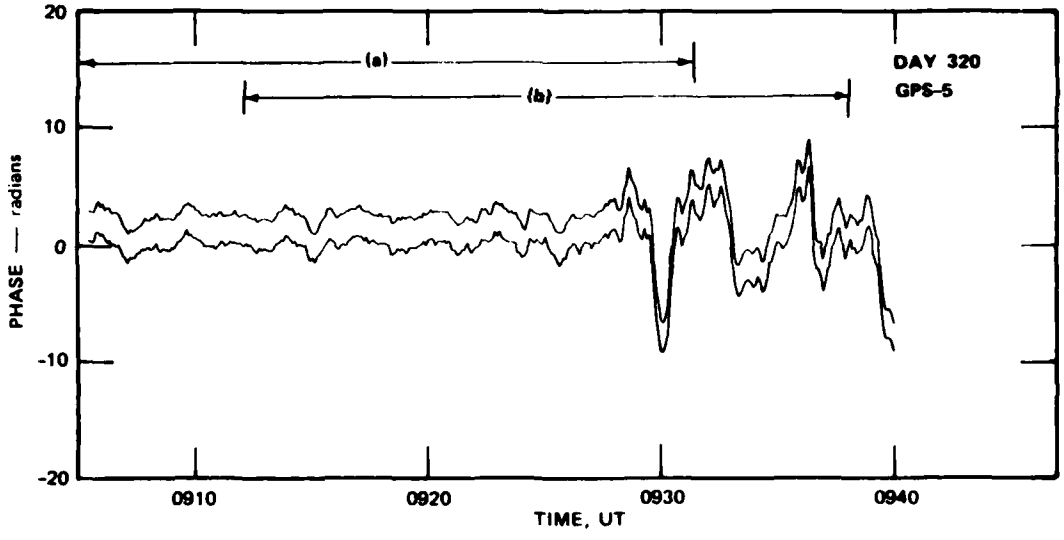

FIGURE 10 GPS SPACED-RECEIVER MEASUREMENTS (DAY 320)

V MULTIPLE BASELINE SPACED-RECEIVER ANALYSIS

A. Introduction

In the conclusion of Section II, we pointed out that an essential element for calculating DFA average beam distortion is irregularity anisotropy because the severity of a propagation disturbance is highly aspect sensitive. The only way to unambiguously establish this anisotropy at the spatial scales important for DFA operation is through the use of multiple-baseline spaced receivers. These same measurements also provide the irregularity drift information required in the calculation of temporal perturbation strength. Thus, if phase scintillation is measured concurrently, as it was for the data discussed here, the final DFA analysis element, turbulence strength, can also be determined.

The application of the spaced-receiver method to measure anisotropy is straightforward. In situ irregularities can generally be characterized in terms of a three-dimensional spatial autocorrelation function; the radio-wave pattern produced at the receiver plane by illuminating those irregularities will, therefore, have a prescribed two-dimensional form. For example, if the in situ irregularities were prolate spheroids, they will produce a diffraction pattern with elliptical contours of constant correlation. By making multiple, simultaneous spatial samples of that diffraction pattern at the receiver plane, correlation techniques can be used to characterize its shape and orientation. By reversing the process, these parameters can be used, in conjunction with a propagation model, to determine the in situ structure.

Similarly, drift measurements using multiple receivers are simple in concept. A frozen diffraction pattern moving across the receiver plane will produce identical signals displaced in time. In the simplest case of an isotropic correlation pattern, dividing the baseline separation by the time delay yields the drift component along that baseline.

In reality, the contributions of anisotropy and drift to the spatial correlation pattern are not directly separable, as discussed in Section III. The interplay between anisotropy and drifts for one measurement geometry is shown in Figure 11. Two differently shaped irregularities are illuminated at an angle relatively close to the direction of magnetic field (i.e., small Briggs-Parkin angle). On the right, the irregularity is field-aligned and rodlike. Projection of the irregularity pattern onto the receiving plane produces a correlation surface with anisotropy lower than that in situ, and, in this case, an alignment near the magnetic meridian. On the left, the irregularity has a second preferred axis along the local L shell, resulting in a sheetlike structure. Because of this magnetic east-west extension, the ground pattern is more highly anisotropic than, and extended in a direction perpendicular to, that for rods.

This example shows how, from a correlation surface characterized in terms of axial ratio and orientation, the two in situ irregularity types can be readily distinguished. Equally important, the example also underscores the need to account for pattern anisotropy before drift information can be extracted from spaced-receiver data. The difficulty is that a high degree of correlation along a particular baseline will be interpreted as a large pattern drift if one simply divides the correlation delay into the baseline length. For rods, the signals at Antennas 1 and 2 are highly correlated with peaks only slightly displaced in time. Interpretation of that small temporal delay as drift produced, without proper correction for pattern anisotropy, would suggest a high north-south drift. Similarly, the sheet-produced pattern would indicate high east-west velocities, which can become infinite if the pattern and baseline are exactly aligned, and would be observed even if the irregularities were not moving. True drift velocity information can be extracted only if the spatial pattern anisotropy is accounted for.

In the results presented in the next section, we have used a correlation method from which pattern anisotropy and true pattern drift can be simultaneously extracted. The technique based upon the work of Armstrong and Coles [1972] and is described in Rino and Livingston [1982]. The method uses the intersections and peaks of all possible cross- and auto-correlation functions derived from three or more antennas. An

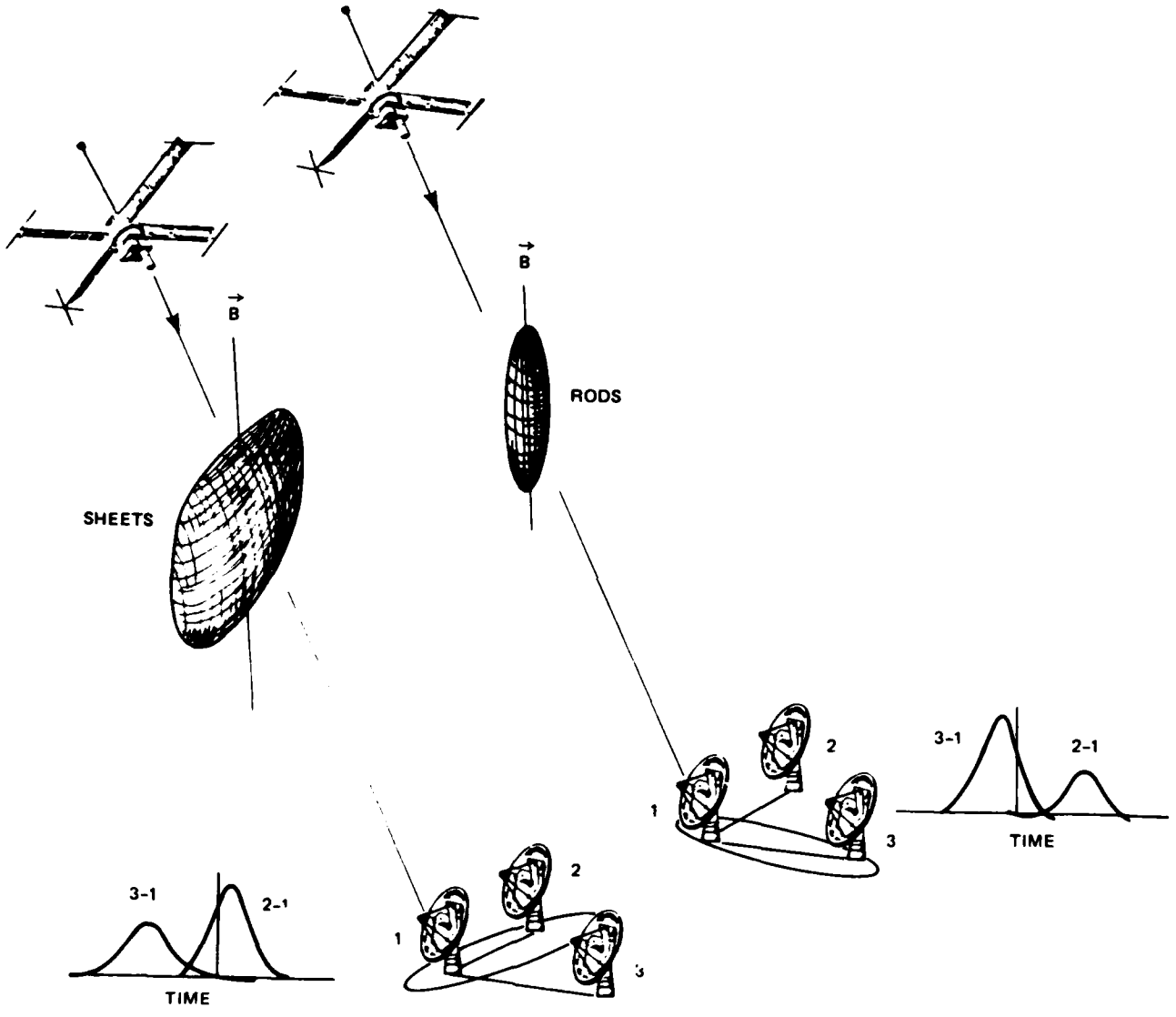

FIGURE 11 AN ILLUSTRATION OF IRREGULARITY ANISOTROPY EFFECTS ON APPARENT DRIFT VELOCITY

over-determined set of linear equations results that is solved for anisotropy and true pattern drift by least-squares methods. The observed values are then compared with model predictions to establish the anisotropy of the scintillation-producing structures. The technique can be applied to signal intensity or to signal phase. The effects of diffraction alter the overall size of the spatial correlation functions of the signal at the receiver, but they do not alter its anisotropy.

Generally speaking, the parameters that describe the signal spatial correlation at the receiver are unique for a particular generic type of irregularity. In our analysis we consider three such types. Field-aligned rods can be described in terms of an axial ratio, a, which is the ratio of the average along-field dimension to the cross-field dimension, and are designated a:1:1. When the irregularities have a second preferred axis perpendicular to the field and along the local L-shell, they are referred to as sheets and are designated a:a:1. Similarly oriented, but nonsymmetrical irregularities, (a:b:1 where b < a) are referred to as wings.

For application to the DFA analysis, we have used data from two very different, but complementary, signal sources. The first of these is the Wideband satellite [Fremouw et al., 1978]. Most of the data from that experiment has been already published, and we will present only summary examples here. Its sun-synchronous, 106-min orbit provided latitudinal scan snapshots of the auroral zone, within a few hours of local midnight, over several seasons of low-to-moderate sunspot conditions. The other signal sources that we have utilized are a series of UHF beacon satellites in highly eccentric orbits and can be observed continuously for a few hours at northern high latitudes. These satellites have been observed from stations in the auroral zone and polar cap routinely since 1979, although we will concentrate on data collected during recent coordinated measurement campaigns. The nature of the data from these latter measurements is quite different from the GPS or Wideband satellite data. For example, the penetration point moves very little, so that the geometrical

propagation factor G (Eq. 31) remains nearly constant and the contribution of satellite motion to the apparent irregularity drift is small, being confined primarily to the radial direction. The temporal behavior of anisotropy and drift at a nearly constsnt latitude can, therefore, be observed daily over a several hour window.

We have presented our examples in two sections. Section V-B discusses the auroral zone and concentrates on anisotropy in the evening and midnight sectors and a comparison between our drift measurements and those made by the Chatanika incoherent-scatter radar. Turbulence strength calculations for strong auroral zone scintillation are also presented. Section V-C presents examples of anisotropy, drifts and turbulence strength, measured in the central polar cap, which provide guidelines for DFA applications at those latitudes.

B. Measurements

1. Auroral-Zone Irregularity Anisotropy and Drifts

Kilometer-scale, scintillation-producing irregularities in the auroral zone have been observed to have a highly variable anisotropy. At these scales, scintillation is enhanced over propagation paths lying along any extended axis of an irregularity [Rino and Fremouw, 1977], a phenomenon that has been used as a diagnostic in comparing measured and predicted scintillation strength as a function of propagation geometry. In the auroral zone, localized enhancements are regularly seen not only where the propagation is along the magnetic field, as produced by rodlike structures, but also when the path lies in the local L shell. Martin and Aarons [1977] explained this occurrence by postulating a second preferred irregularity axis, i.e., L-shell-aligned sheets. Rino and Matthews [1980] and Basu et al. [1981] arrived at a similar conclusion using scintillation enhancements from the extensive Wideband satellite data base. Observations from both the Pacific and Atlantic sector auroral zone were included in these latter studies. Unfortunately, the method depends upon scintillation enhancements being totally attributable to geometry. Accordingly, the results can be ambiguous if irregularity strength is not constant with latitude and time.

Moorcroft and Arima [1972] were the first to determine anisotropy from spaced-receiver data in the auroral zone. They found evidence of sheetlike structures, but with meridional alignment. More recently, Rino and Livingston [1982] present evidence of sheetlike and winglike structures, derived from Wideband spaced-receiver data. This confirmed the occurrence of sheets demonstrated earlier by Rino et al. [1978], based on spaced-receiver analysis of data recorded at Poker Flat, Alaska.

A more complete study of anisotropy was recently made by Livingston et al. [1982], also based upon Wideband data. They established that auroral-zone anisotropy depends upon both latitude and local time and appears to be convection dominated. Figure 12 is a reproduction of one of their summary plots, which corresponds to moderate magnetic and sunspot number conditions. In the pre- and post-midnight sectors, the north-to-south latitudinal progression is from nearly isotropic irregularities to rods with increasing elongation. These give way to sheets in a narrow latitudinal sector corresponding to the equatorward edge of the aurora. Just before local midnight, the anisotropy of the rods lessens, and the sheets become wings. Livingston et al. [1982] interpret this pattern by the Harang discontinuity [Heppner, 1972]. To indicate this process, the large-scale flow pattern expected for this level of magnetic activity has been superimposed. We emphasize that this is a model pattern.

Figure 12 suggests that the sheets and wings are most prevalent within an hour or two of local midnight. Unfortunately, the Wideband orbit was such that the presence of sheets in the evening or morning sectors can be neither confirmed nor denied. (It has been established, however, that during the hours around local noon no sheets or wings are observed.)

The question of whether sheets occur in the evening or morning auroral zone is important both to understanding of irregularity generation mechanisms and the DFA pertinent morphology. The data from the high-eccentricity-orbit signal sources previously mentioned, helps fill this local time gap. For the November 1981 Chatanika radar campaign, between 1800 LT and 2100 LT, the geometry to those sources was favorable for

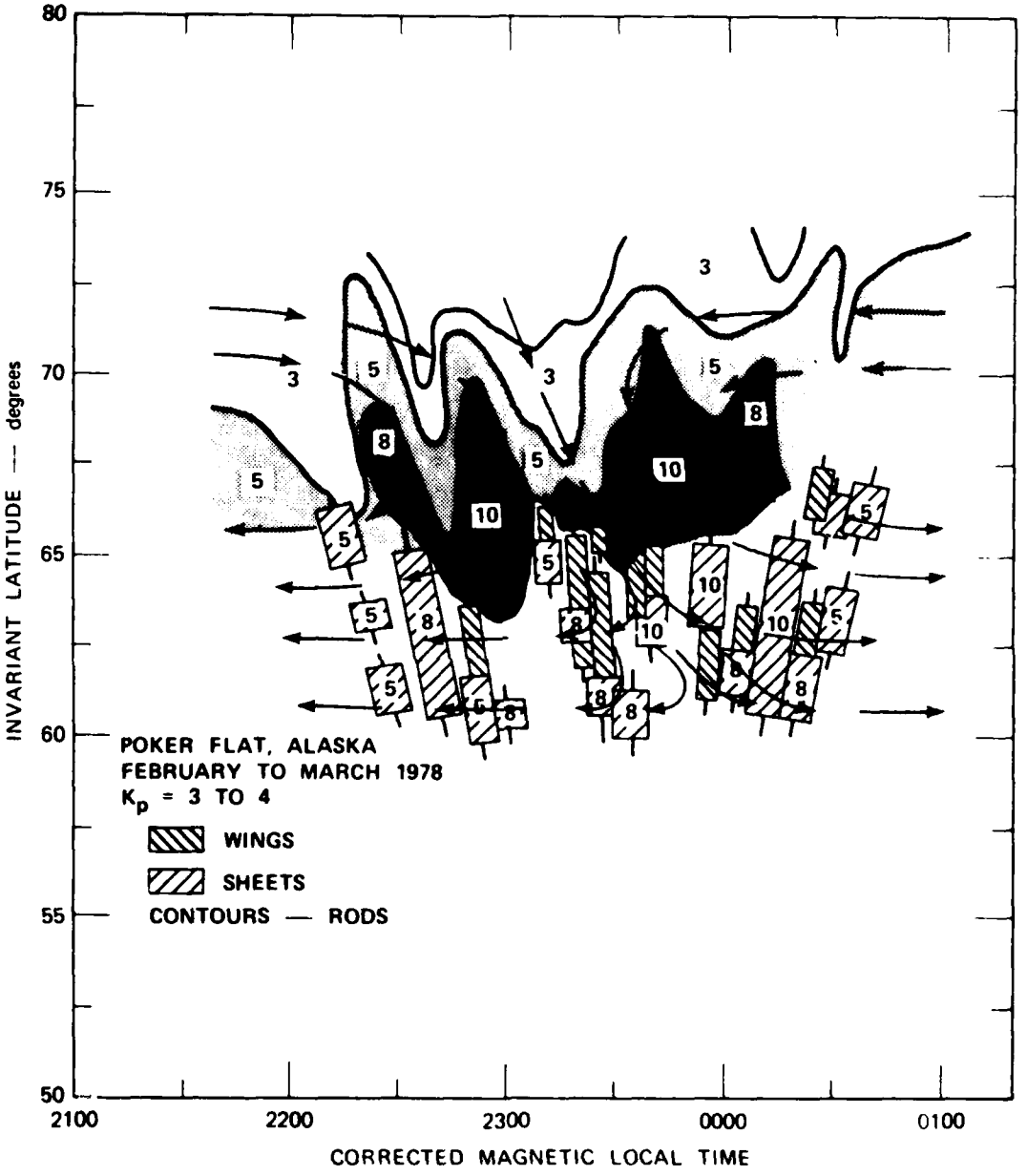

FIGURE 12 AVERAGE AURORAL-ZONE IRREGULARITY ANISOTROPY FROM THE WIDEBAND EXPERIMENT

detailed anisotropy and drift measurements. During the more recent, February-to-March 1982 campaign, also at Chatanika, the optimum geometry occurred in the local morning sector.

Our discussion here will concentrate on the first of these campaigns, during which the GPS data already discussed was collected. This includes data that directly overlap the Wideband data of Figure 12, so that the temporal variation of anisotropy and drift on one evening can be directly compared with the long-term morphological pattern. We have also included measurements that were coordinated with incoherent-scatter radar observations. This provides an opportunity to (1) establish the irregularity anisotropy at intermediate spatial scales and associate changes in the structure with large-scale plasma features observed by the radar, and (2) compare radar-measured plasma drifts with those of the intermediate scale, scintillation-producing structures.

We will first consider the midnight sector beacon measurements. Figure 13 shows the correlation pattern axial ratio and orientation measured on Day 315, 1981, for a low-elevation, northward-looking geometry. Superimposed on the measurements are the model predictions for 5:1:1 rods and 5:5:1 sheets. For this geometry it is impossible to distinguish the two irregularity types from pattern orientation alone. The axial ratio data, however, do provide information about the in situ structure. Sheets, illuminated broadside produce a near-isotropic correlation pattern, while rods have an extended shadow. The measured axial ratio data is systematically higher than that for sheets, but lower than that for 5:1:1 rods, indicating an overall in situ anisotropy of about 3:1:1.

Because they overlap in latitude and local time, we can compare the anisotropy pattern in detail with the Wideband measurements. The in situ anisotropies implied from the model-measurement comparisons have been mapped in Figure 14 in the same format as the Wideband data. To facilitate the comparison with Figure 12 and to indicate the convection process that we believe controls the anisotropy, the expected large-scale flow pattern is superimposed on Figure 14. Both Figures 12 and 14 correspond to moderate magnetic conditions (k_p = 3 to 4) and should therefore be

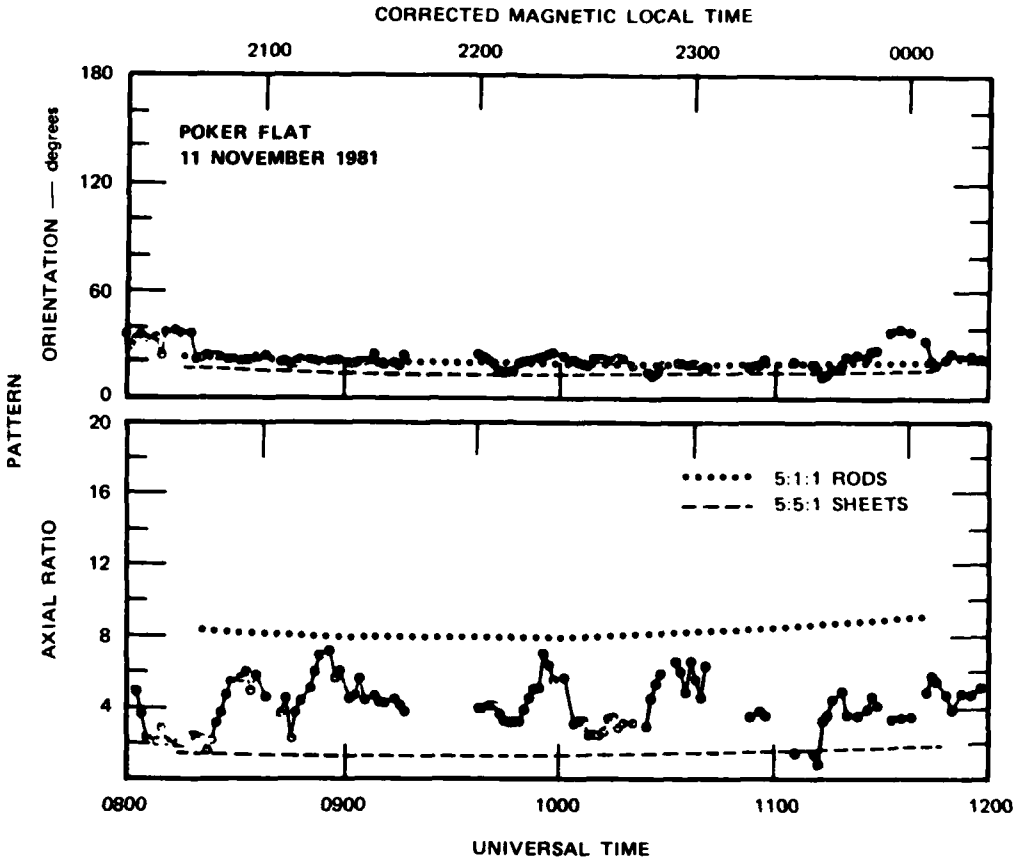

FIGURE 13 MEASURED AND MODEL PATTERN ANISOTROPY

directly comparable in terms of the latitudinal and local magnetic time dependence of anisotropy. We do, in fact, see a consistent behavior between the two. A local-time cut through Figure 12 at an invariant latitude of 70° shows a pattern of rods ranging from 3:1:1 through 5:1:1 with short peaks of 8:1:1 elongation near 2220 and 2350 MLT. This is very similar to the anisotropy pattern of Figure 14 where peaks of 5:1:1 rods near 2230 and 0000 MLT are observed. The minimum in irregularity elongation is not quite as distinct in the Day 315 data, nor is the generally higher anisotropy post- versus pre-midnight. These differences, and the generally lower values of anisotropy, are most likely statistical. On the other hand, it may indicate that spatial scale size depends slightly on anisotropy. For Wideband, the scales sampled are in the 1- to 2-km range, as dictated by the phase detrend cutoff. The beacon data corresponds more nearly to

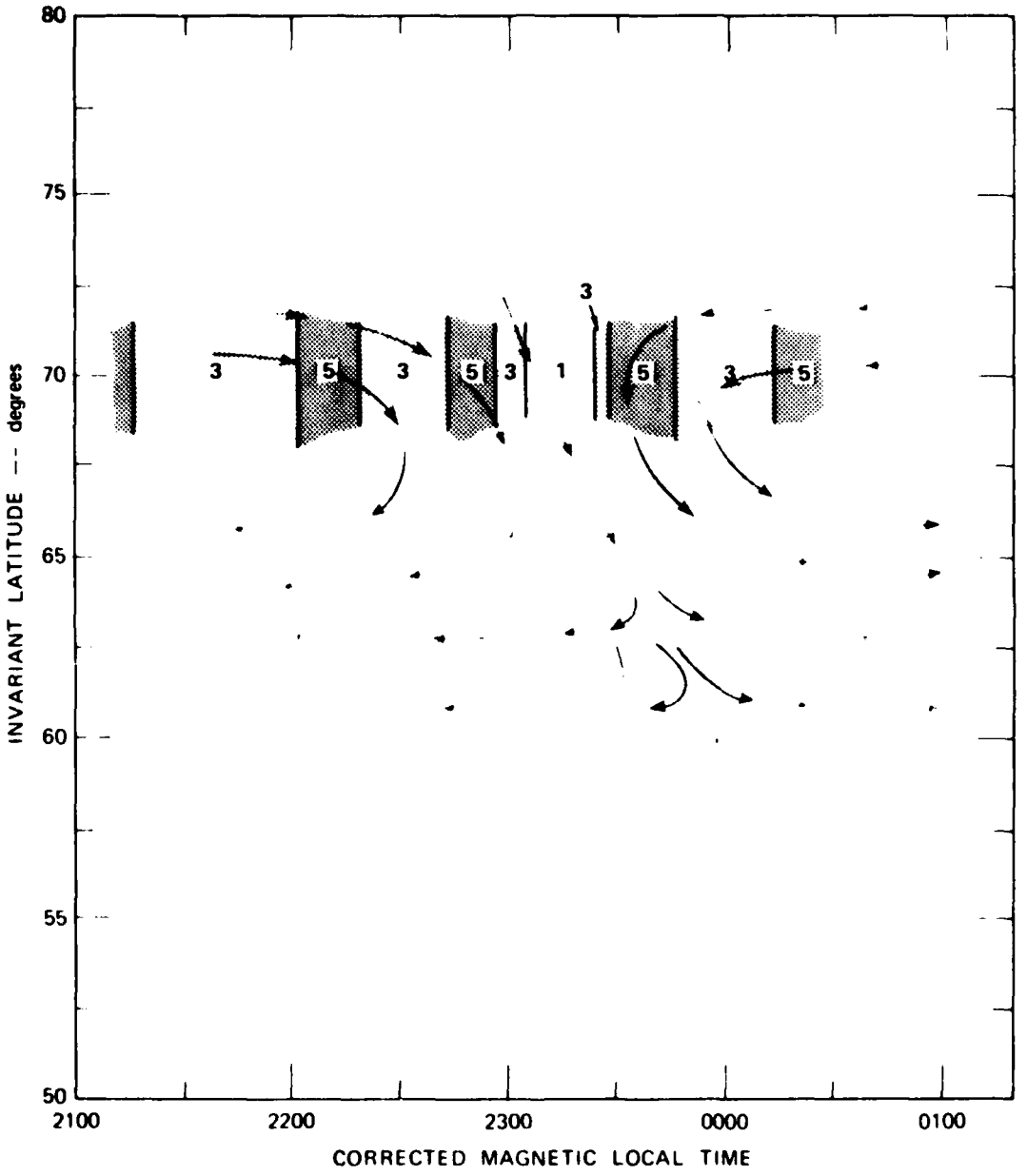

FIGURE 14 MEASURED IRREGULARITY ANISOTROPY

0.5 km, which is near the signal intensity Fresnel radius cutoff for the observation frequency and geometry.

In Livingston et al. [1982] it was postulated from the anisotropy pattern that the irregularity structure was controlled by convection. With the UHF polar-beacon data, where velocities are simultaneously extracted, it is possible to test this hypothesis directly. The drift data are plotted in Figure 15. We emphasize that these are true (not apparent) drift velocities from which the pattern anisotropy has been removed. Superimposed on Figure 15 is the same Harang discontinuity pattern used in Figures 13 and 14. As can be seen, the data in Figure 15 match the predicted large-scale flow pattern remarkably well. Before 2300 CMLT, the drift is about 250 m/s eastward and switches to about 300 m/s southward by local midnight.

To demonstrate auroral zone anisotropy and drifts in a local time sector which Wideband did not sample, we now turn to data collected from a different polar beacon early in the evening of 11 November 1981. The F-region penetration latitude for these data is near 65° invariant or near the poleward edge of the sheet-wing region in Figure 13, although as we have said, the two experiments do not overlap in local time.

Figure 16 shows the measured correlation pattern anisotropy and orientation for this evening, and the superimposed model predictions for 5:1:1 rods and 5:5:1 sheets. Unlike the lower elevation geometry of Figure 13, the rods and sheets produce patterns that are significantly different in orientation. Note that extending the rod and sheet dimensions beyond that used here will not alter the correlation surface orientation, although it will alter the observed pattern axial ratio. Figure 16 indicates that during the observation period the in situ irregularities are rodlike. At no time does the orientation deviate systematically from the rod pattern towards that for sheets. The axial ratio does vary, however, corresponding to in situ rod extensions from a minimum of 5:1:1 to a maximum of 15:1:1. Incidentally, these changes seem to be associated with the passage of macroscale plasma enhancements seen in the radar data, although a detailed correlation has yet to be made.

Because these and the Wideband data cannot be directly compared, it is difficult to say whether the absence of sheets in the polar beacon

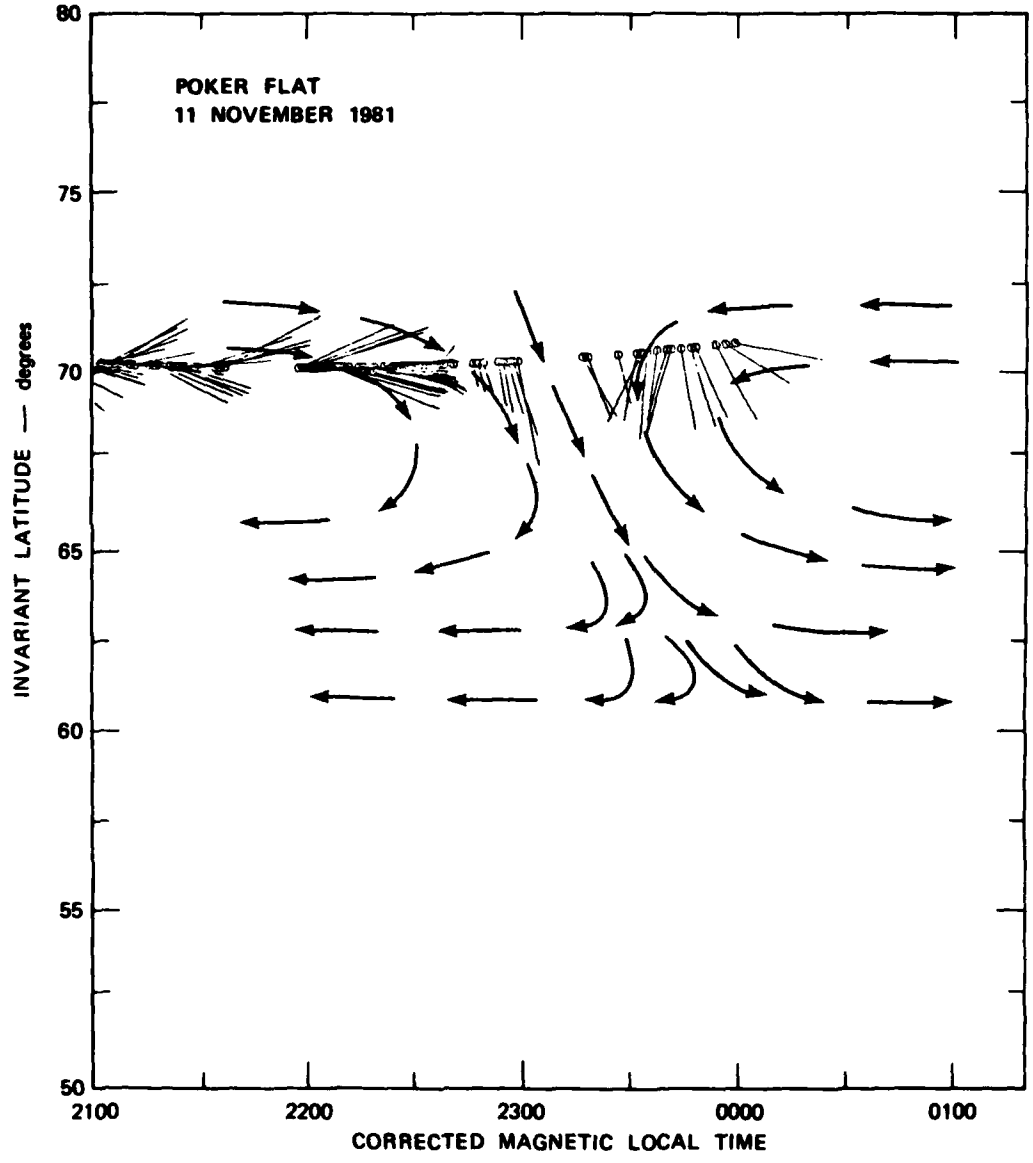

FIGURE 15 MEASURED IRREGULARITY DRIFTS

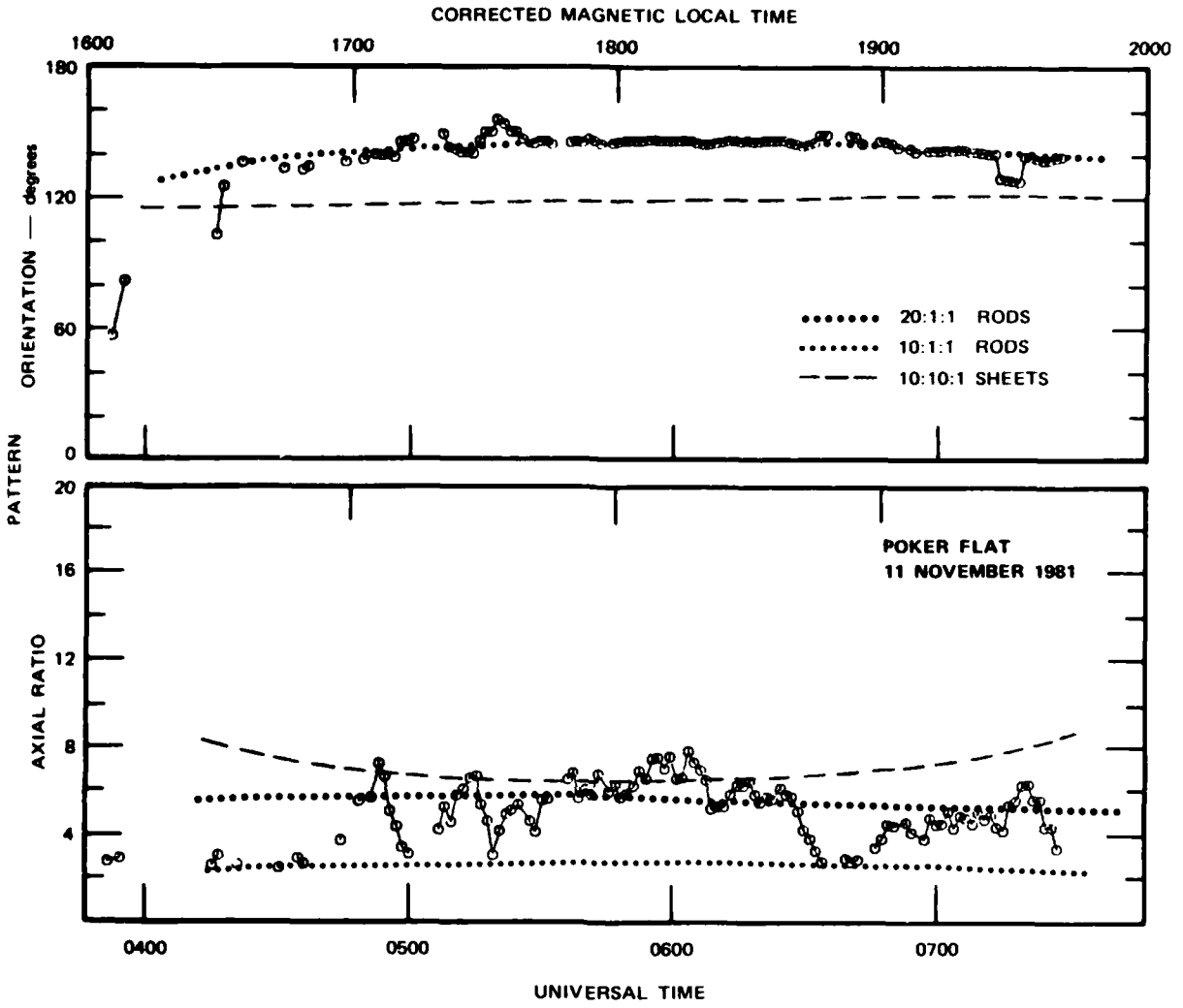

FIGURE 16 MEASURED AND MODEL PATTERN ANISOTROPY

data can be attributed to a local time or latitudinal dependence. We note, however, that the in situ anisotropy is higher for this near-overhead geometry than to the north later in the evening. In this sense, the latitudinal behavior of the degree of rod elongation is consistent between the evening sector and the midnight sector data of Figure 12.

An advantage of the near-overhead geometry for this data set is that the simultaneously extracted irregularity drifts can be compared with radar-measured plasma drifts. The spaced-receiver drift data is shown in Figure 17, rotated into magnetic coordinates. These are, again, corrected

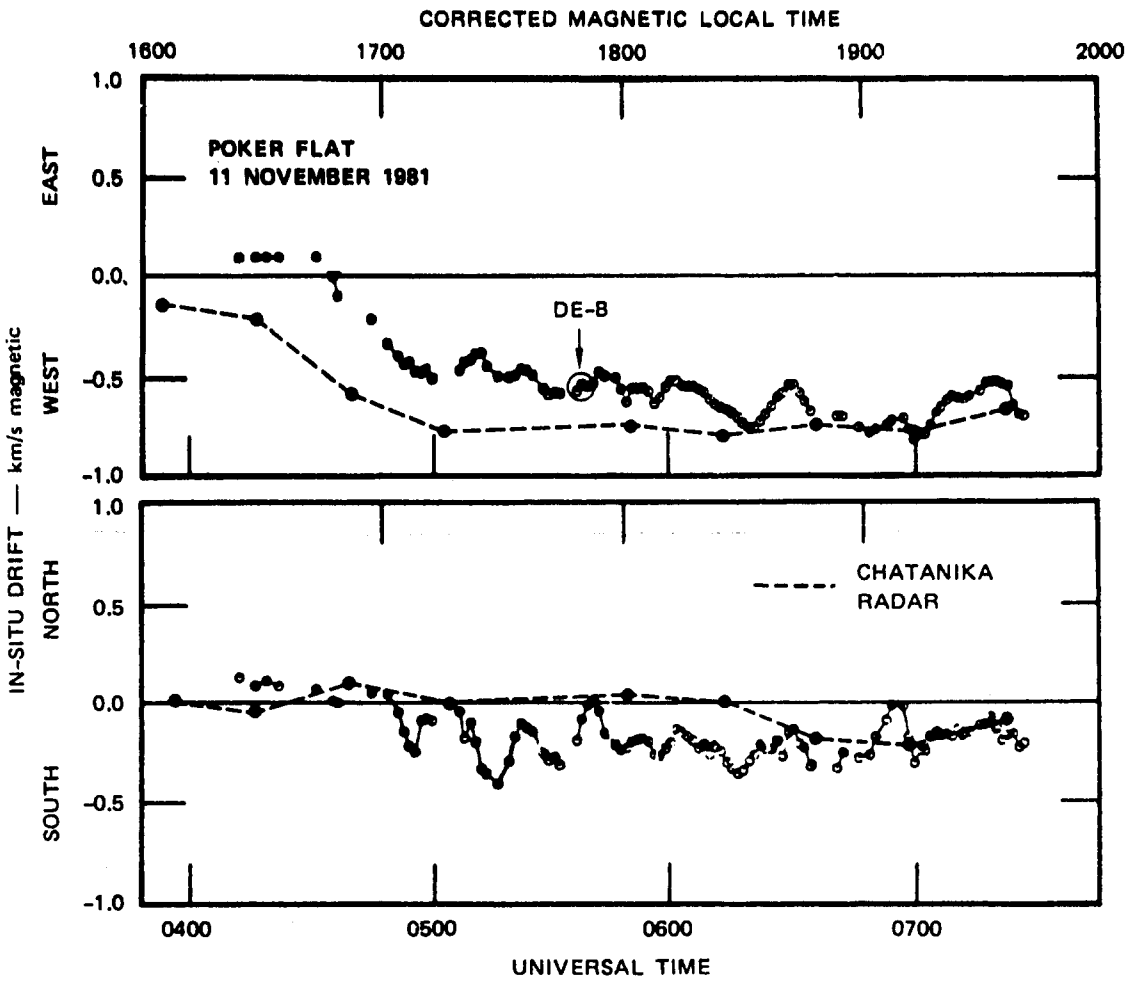

FIGURE 17 MEASURED IRREGULARITY DRIFT COMPARISON WITH CHATANIKA RADAR AND DE-B SATELLITE DRIFT DATA

for pattern anisotropy and peak at nearly 800 m/s westward near 1900 CMLT. The corresponding apparent velocities, that is, those obtained by dividing the correlation peak delays into the baseline length, routinely exceed 2000 m/s. Clearly, interpretation of the apparent velocities as true drifts leads to serious error.

The Chatanika radar F-region plasma drifts are superimposed on Figure 17. These values are those measured at the same penetration latitude as the satellite data and are derived by combining elevation scan pairs: one in the meridian and one to the west at the same magnetic local time. As the map in Figure 18 illustrates, these scans bracket the satellite penetration point in longitude; the duration of the scans

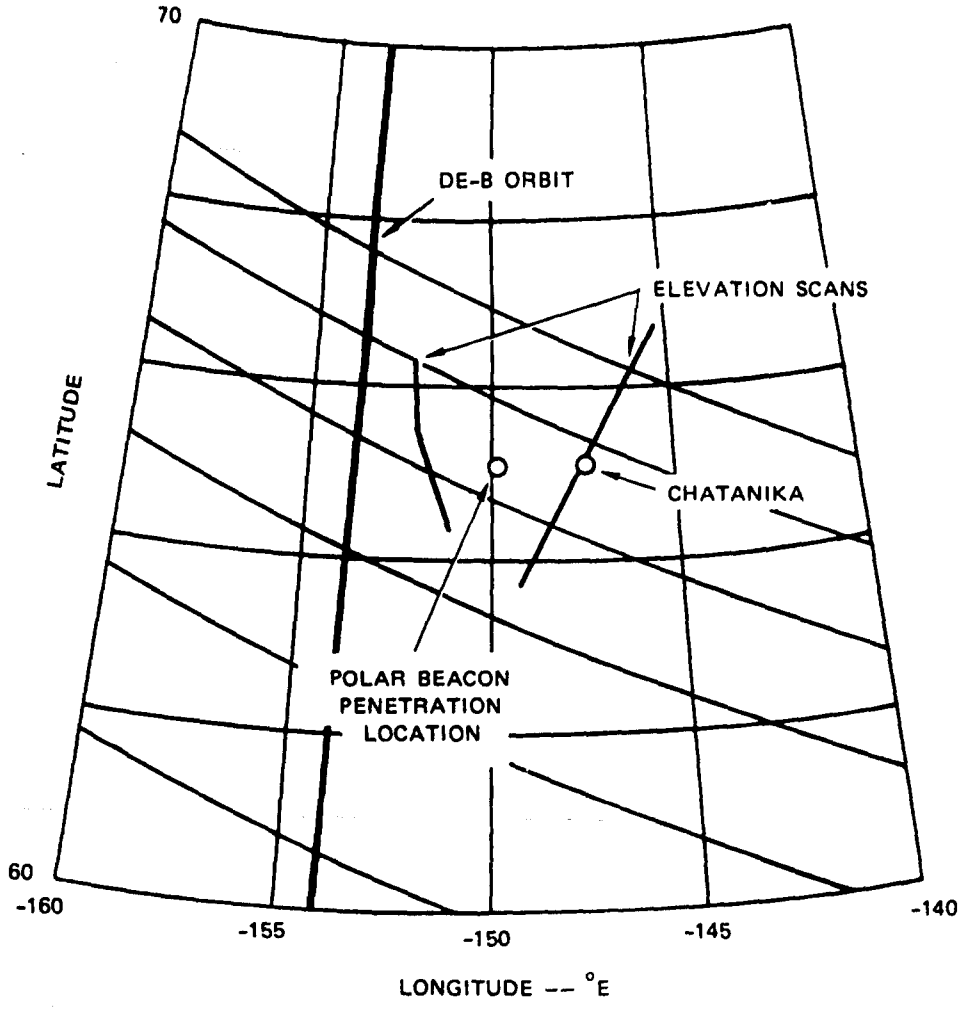

FIGURE 18 MAP OF THE MEASUREMENT GEOMETRY FOR COMPARISON OF SPACED-RECEIVER, RADAR, AND IN-SITU DRIFT MEASUREMENTS

gives a single velocity about every 25 min, while those from the scintillation measurements are about every 1.5 min.

The north-south drift is low as expected for the local evening sector. The two measurements match well, although the spaced-receiver system provides much more temporal resolution. The radar indicates a strong westward drift, which eventually exceeds 800 m/s starting about 1700 CMLT, and which corresponds to the passage of a 500-γ positive bay. The spaced-receiver drifts show a very similar temporal pattern, although initially the westward irregularity drift is much smaller in magnitude than that measured by the radar. The biggest difference between the two measurements occurs near 1715 CMLT, when the westward irregularity drift

is about 60 percent of the plasma drift magnitude; by 1900 CMLT, the two measurements match very well. Two explanations can be offered for the early time discrepancy. The validity of the radar measurement depends upon homogeneity across the several degrees of longitude separating the scans. This condition may not be satisfied during the initial passage of the magnetic disturbance, leaving the radar measurements questionable. After about 1830 CMLT, when the disturbance has passed and longitudinal homogeneity is restored, the measurements agree.

Alternatively, the irregularity drifts can include the effects of local polarization fields if the density enhancement within the irregularity is strong. For example, if the north-south polarization field produced by the irregularities were in the order of 10 m^V/m, the westward drift of the irregularities at our 600 m spatial scale would be reduced by about 150 m/s from that of the plasma. Under the right conditions, a large-scale density enhancement of 3×10^6 could alter the field this much (Tsunoda, private communication) although quantitative estimates of the effect would be difficult, particularly the effects of lower ionosphere conductivity. For either mechanism, the scenario agrees well with the plasma conditions seen by the radar. Up through 1715 CMLT, the ionosphere is relatively uniform. Between that time and 1900 CMLT, a number of 100-km scale density enhancements structured in latitude and longitude drift through the sampled region and then disappear to the south.

A second velocity comparison can be made with these data using the Dynamics Explorer satellite (DE-B), which passed the penetration latitude to the west of Chatanika as shown in Figure 18. The in situ measurement technique is described by Heelis et al. [1981]. During the satellite pass, which occurred near 1805 CMLT, we can assume that the horizontal drift component is purely magnetic westward from the satellite orbital inclination and the dominance of the westward drift. The magnitude of the DE-B measured drift is about 600 m/s, although velocity increases a few degrees south in latitude. This single comparison point is indicated in Figure 17 and matches the spaced receiver derived value almost exactly. Because the in situ probe responses to local fields, better agreement with the spaced-receiver measurement than with the radar data could be expected.

In conclusion, the auroral zone spaced-receiver measurements have provided anisotropy and drift data directly applicable to the DFA problem. The validity of the drift extraction technique has been proven by comparison with radar and in-situ data. In the midnight sector, the anisotropy variations with latitude and local time have been established using Wideband data, and verified by the polar beacon observations. In the early evening sector, the temporal behavior of anisotropy in the central auroral zone has been measured. The agreement between our drift measurements and classical flow patterns, and the apparent convective control of anisotropy suggests that the application of a global model for DFA analyses should be straightforward.

2. Auroral-Zone Turbulence Strength and DFA Limitations

The night of 11 November 1981, on which the anisotropy and velocity observations in Figure 4 and 5 were made, was also a period of strong intensity and phase scintillation. The S_4 intensity scintillation index at 244 MHz was in or near saturation for two hours near midnight and roughly corresponds to the maximum scintillation levels observed by the Wideband experiment at the same propagation geometry. If coupled with field-aligned propagation geometries and high plasma velocities, this strong irregularity turbulence may represent near-worst case condition for DFA application in the auroral zone.

The starting point for the calculation of turbulence strength, C_s, (Eqs. 30 through 33) is the measured phase spectral density. The strongest scintillation periods on 11 November correspond to average phase spectral strength, T = -18 dB, and spectral index, p = 2.9. In addition to these measured parameters, we have assumed (1) rodlike irregularity anisotropies of between 5:1:1 and 10:1:1, typical of those measured, (2) a plasma drift velocity of 800 m/s, which is near the maximum observed during the period, and (3) a scattering layer thickness of 100 km. For the propagation geometry of the observations, this results in a value of $C_s \cong 10^{20}$. It is interesting to note that this level is near the median value observed at the magnetic equator during moderate sunspot number, disturbed evening conditions [Livingston et al., 1981]. This is consistent with the Wideband satellite observations, which

showed consistently weaker scintillation in the auroral zone than at the equator, particularly as the sunspot activity increased.

The degree of DFA beam distortion can be estimated by calculating the spatial decorrelation contour described by Eq (21). We consider two propagation situations. The first of these is for the observed average axial ratio of 5:1:1 rods and the actual observation geometry. The second case is for field-aligned propagation and the peak observed axial ratio of 10:1:1. This second situation is worse-case in two regards. The propagation factor G peaks at field alignment so that the perturbation strength maximizes. In addition, the spatial correlation pattern is nearly isotropic so that decorrelation is equally rapid in all directions.

The 1/e spatial decorrelation contour for these two propagation situations is shown in Figure 19. For reference, two radio wavelengths

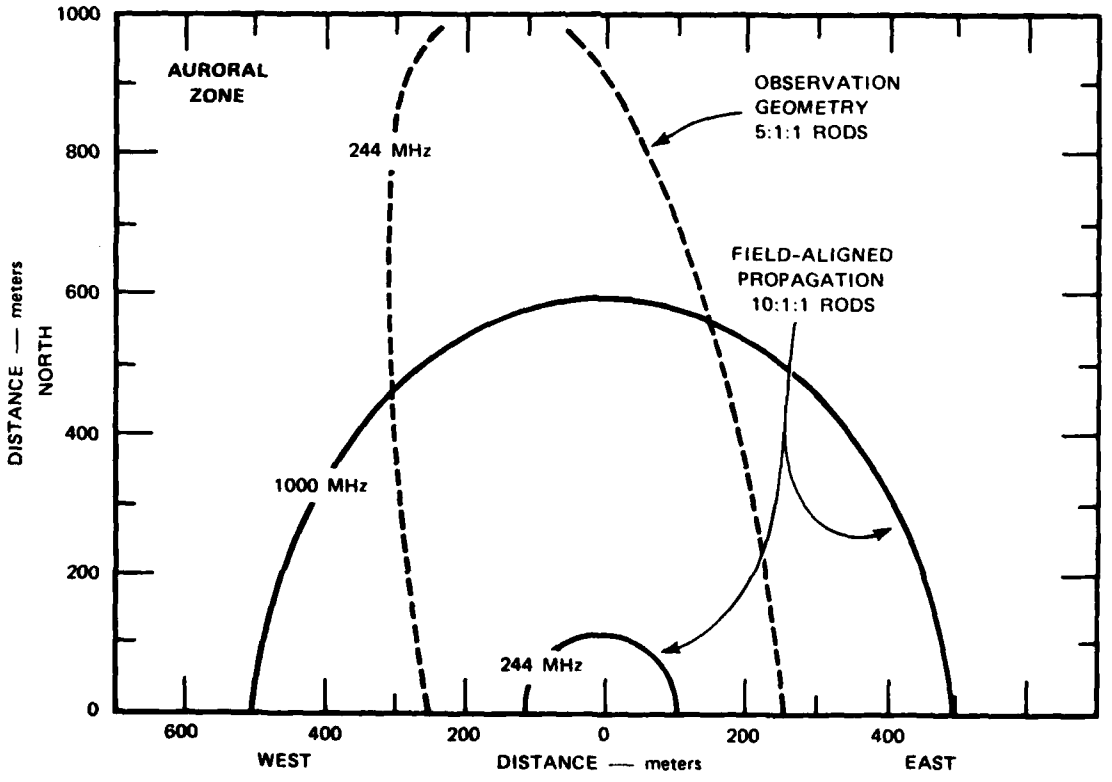

FIGURE 19 PREDICTED SPATIAL-DECORRELATION PATTERN

have been used: one is the observation frequency and the other is 1000 MHz. For the observation geometry the decorrelation scale is large; for the higher frequency the 1/e contour is beyond the limits of the figure. At 244 MHz, the contour is, of course, smaller and exhibits the pattern anisotropy expected for the azimuth of observation.

The field-aligned, near-vertical geometry cases are more pertinent to DFA applications. Propagation along the extended axis of the irregularities symmetrizes the spatial correlation and reduces the decorrelation scale at 244 MHz to about 100 m. At 1000 MHz, that dimension is about 500 m. For our purposes here, it is adequate to say that significant distortion of the desired DFA beam should be expected if the aperture dimensions at 244 MHz or 1000 MHz approach these decorrelation scales. Specific calculation of sidelobe degradation will be discussed in Section VI.

We can extrapolate from the contours in Figure 19 to other irregularity anisotropies and turbulence strengths. For example, L-shell-aligned propagation through sheetlike irregularities will produce a spatial correlation surface narrow along one axis, but extended along the other. The narrow dimension will have a decorrelation scale similar to that for field-aligned propagation and rodlike irregularities. As for changes in turbulent strength, the correlation contour narrows in all directions by roughly a factor of two from that in Figure 9, for a 10-dB increase in C_s. In the auroral zone, systematic increases of this magnitude seem unlikely, however.

3. Polar-Cap Anisotropy and Drifts

The magnetic polar cap is the region of open magnetic field lines that, driven by the solar wind, extends into the tail of the magnetosphere. It is, accordingly, a region in which the structure and dynamics are closely tied to the state of the interplanetary magnetic field (IMF) and thus to the sun. This solar control is conspicuous if we consider the scintillation changes observed over the recent sunspot cycle. A measurement campaign in 1975 judged the region benign in terms of communication disruption, but in 1979 scintillation levels throughout

the local winter routinely exceeded those simultaneously observed in the auroral zone [Aarons et al., 1981].

The polar-cap region is interesting not only because of the severity of scintillation, but it is, very likely, a source region for the large-scale electron-density structures observed in the auroral zone. Furthermore, the dynamics of the region provide a sensitive indicator of the sense and magnitude of the interplanetary magnetic field. These factors are essential to an understanding of the irregularity physics and to the eventual goal of global DFA modeling.

Until the observations that are discussed here were made, virtually no measurements of intermediate-scale irregularity anisotropy in the polar cap existed. The occasional exceptions are from the early portions of Wideband satellite passes in the midnight sector and under disturbed magnetic conditions; however, the low-elevation-angle-observation geometry for these Wideband cases is far from ideal for the detailed diagnosis of irregularity shape. In contrast with this lack of anisotropy data, the plasma drift in the polar cap has been extensively studied using both modeling and observation. Experimental concentration has been on the large-scale electric-field patterns mapped down from the magnetosphere. These have been implied from multiple magnetometer data [Friis-Christensen et al., 1972] or directly measured by balloon flights [Mozer and Serlin, 1969] and satellites [Heelis et al., 1981].

The polar-cap plasma flow direction is dominated by the northward (B_Z) component of the interplanetary field. Under normal conditions, B_Z is negative and small, this results in a convection pattern in the vicinity of the magnetic pole that is two-celled with flow from noon towards midnight and sunward return through the dawn and dusk auroral zones. Generally, the two-flow cells are asymmetric, both skewed from the noon-midnight meridian, and offset from the magnetic pole. This lack of symmetry is generated by spatial or temporal changes in the eastward component of the IMF, B_Y, which to first order controls the dawn-dusk flow component.

When B_Z turns northward, a variety of complex electric-field distributions can occur. Heppner [1972] has categorized these in terms

of their dawn-dusk signatures. These range from patterns explainable by four-celled polar-cap convection to essentially random field variations throughout the entire region. Burke et al. [1979] have studied a subset of B_Z north observations and have postulated a magnetospheric mechanism for their cause.

Satellite in situ measurements of polar-cap electric fields such as those referenced above have been made using sun-synchronous dawn-dusk orbits. These provide one-dimensional snapshots of the most critical features of the convection dynamics, but cannot provide simultaneous information about the field elsewhere in the polar cap. The power of the ground-based drift measurements using the polar beacons is that the drift pattern can be continuously monitored, albeit at a single point. The complimentary nature of the two methods is clear, and should be taken full advantage of when possible.

The data we discuss here are from an extensive spaced-receiver data set collected from Thule, Greenland. Since 1979, short spans of multiple antenna observations have been routinely made daily for several months at a time; our emphasis here is on data from several days of continuous observations made during January 1982. The diurnal drift patterns derived from these data, using signals from the UHF polar beacons, is currently being consolidated. Here we present anisotropy and drift data for one consecutive dawn, noon, and dusk sequence during which the magnetic-field conditions were nearly constant.

Dawn-sector anisotropy data for 22 January 1982 is shown in Figure 20. The lower scale on the figure is universal time while the upper scale indicates corrected magnetic local time. Because the penetration point remains nearly constant during the observations, the two time scales are separated by a fixed amount. The invariant latitude at F-region penetration altitudes is near 85°, well into the central polar cap.

The ground-diffraction-pattern orientation data in the top portion of Figure 20 distinctly indicates rodlike irregularities as the cause of the scintillation. In fact, the model predictions cannot be

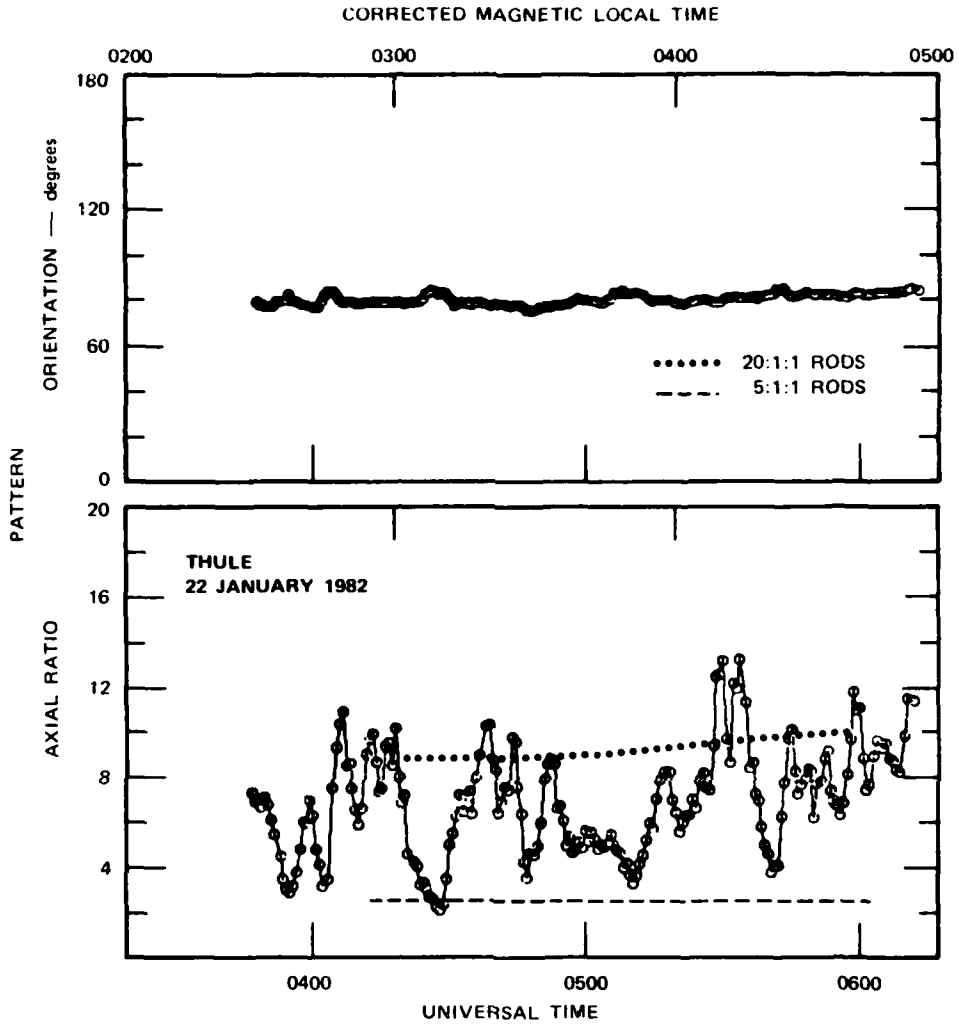

FIGURE 20 LOCAL-DAWN-SECTOR MEASURED AND MODEL PATTERN ANISOTROPY

distinguished from the measured data; those for sheetlike irregularities (not shown) differ by nearly 30° from the measured orientation. The irregularity extension, for which two model predictions are shown, is quite variable, but generally is greater than that seen in the auroral zone [Livingston et al., 1982], reaching 20:1:1 beyond 0530 UT. The corresponding dawn-sector drifts are shown in Figure 21. The drift magnitudes are high, and exceed 900 m/s slightly past 0500 UT. The magnetic north-south component systematically increases from 200 m/s to about

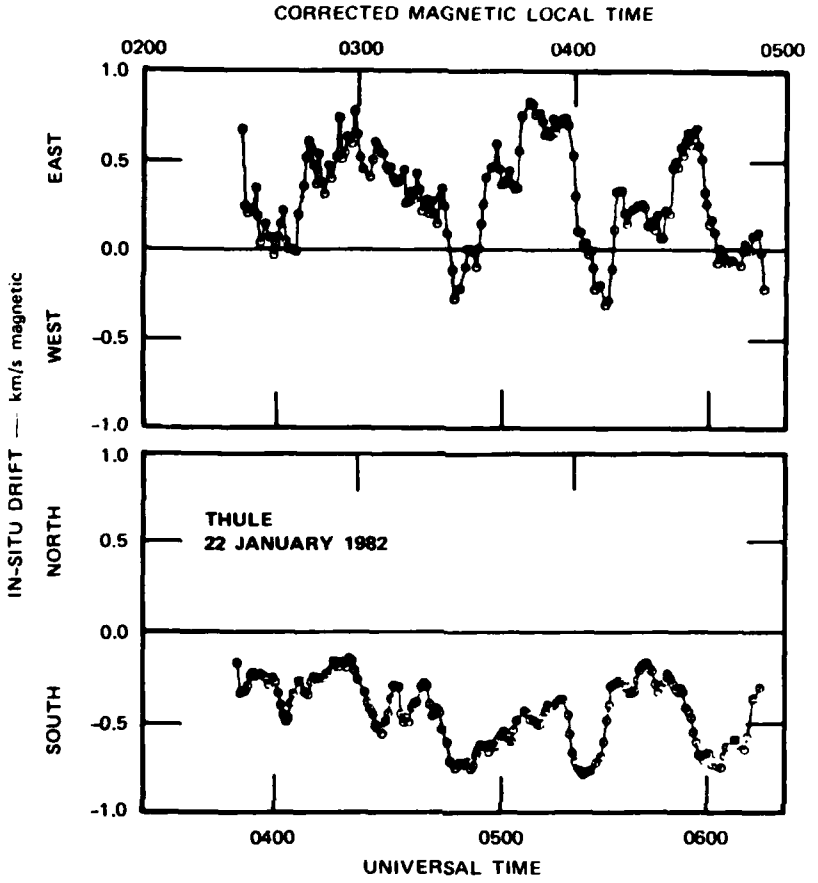

FIGURE 21 LOCAL-DAWN-SECTOR MEASURED IRREGULARITY DRIFTS

500 m/s southward, while the more rapidly varying east-west component averages about 400 m/s in an eastward direction. For this invariant latitude, the southeastward flow is consistent with an overall two-cell flow pattern expected for B_Z negative conditions. A comparison of Figures 20 and 21 suggests the same convective control of anisotropy observed in the auroral zone [Livingston et al., 1982]. Generally, the axial ratio follows the variations in north-south drift, minimizing when the drifts are high. The association between anisotropy and the east-west velocity component is not clear. This point will be discussed further in association with the noon- and dusk-sector data.

The local-noon-sector data correspond to nearly the same invariant latitude of 85° and are shown in Figures 22 and 23. The irregulari-

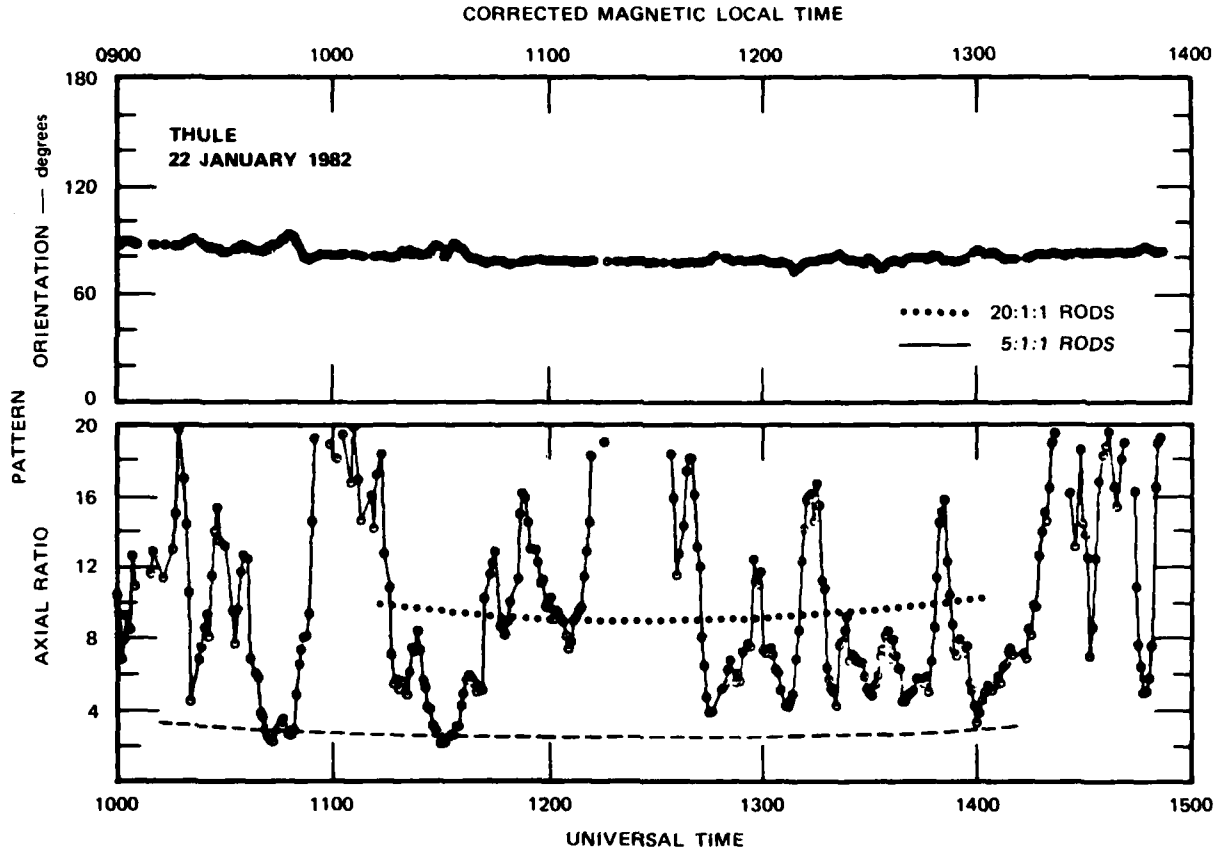

FIGURE 22 LOCAL-NOON-SECTOR MEASURED AND MODEL PATTERN ANISOTROPY

ties are still rodlike, but are extended over those seen in the dawn sector, and exceed 50:1:1 at times. An in situ extension of 20:1:1 is a typical value. The axial ratio varies with a 60-to-80-min period up through 1300 UT, perhaps associated with the passage of F-region sun-aligned arcs [Weber and Buchau, 1981]. The drifts in Figure 23 are mostly antisunward, as expected in the noon sector, but also include a distinct, but rapidly varying westward component. This presumably arises from an asymmetry in the two-celled pattern generated by a nonzero component of B_Y. The magnitude of the drifts occasionally exceeds 800 m/s, and are, therefore, comparable to those observed in the dawn sector. Unlike the dawn sector, however, the variations in axial ratio are tied more closely to changes in east-west drift.

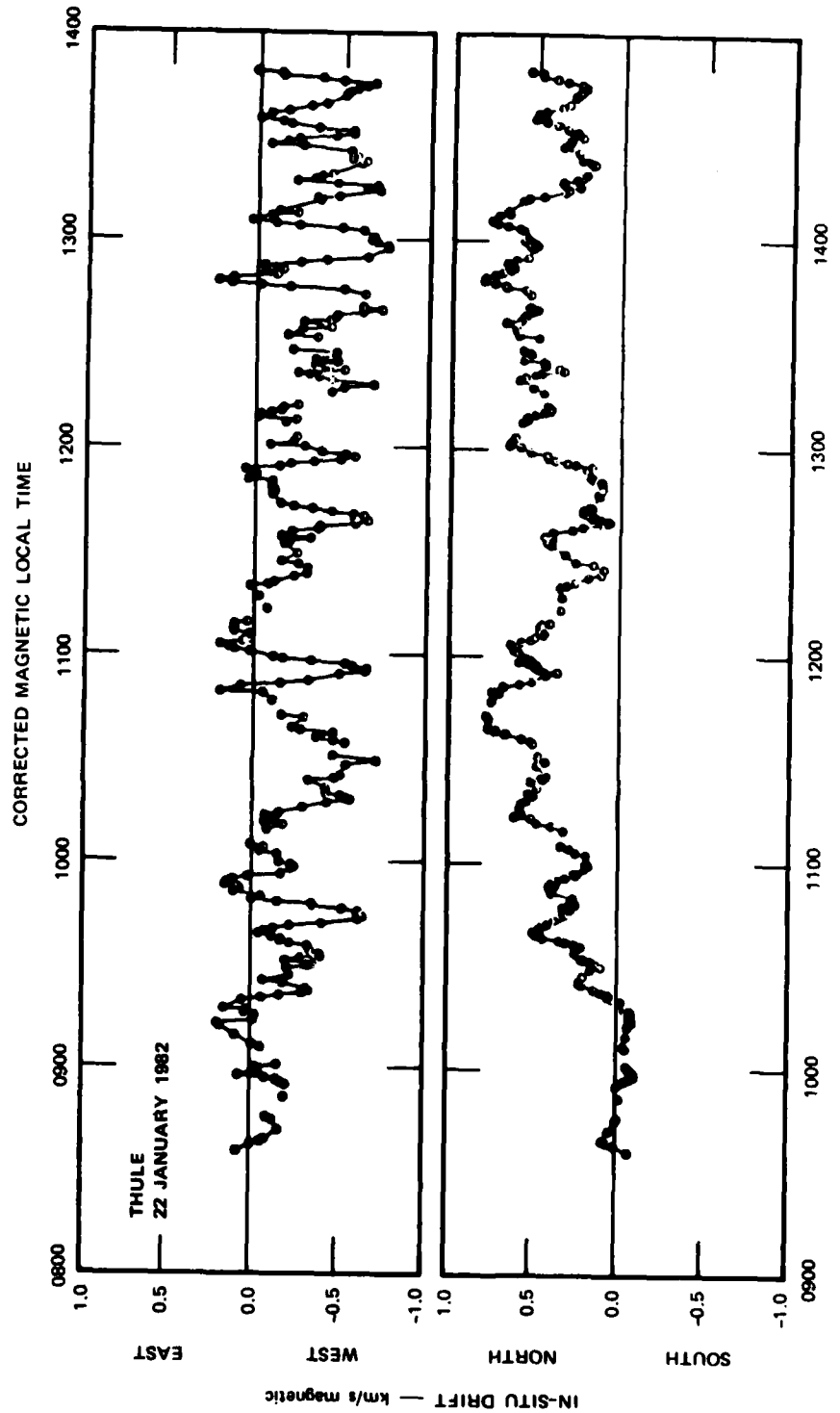

FIGURE 23 LOCAL-NOON-SECTOR MEASURED IRREGULARITY DRIFTS

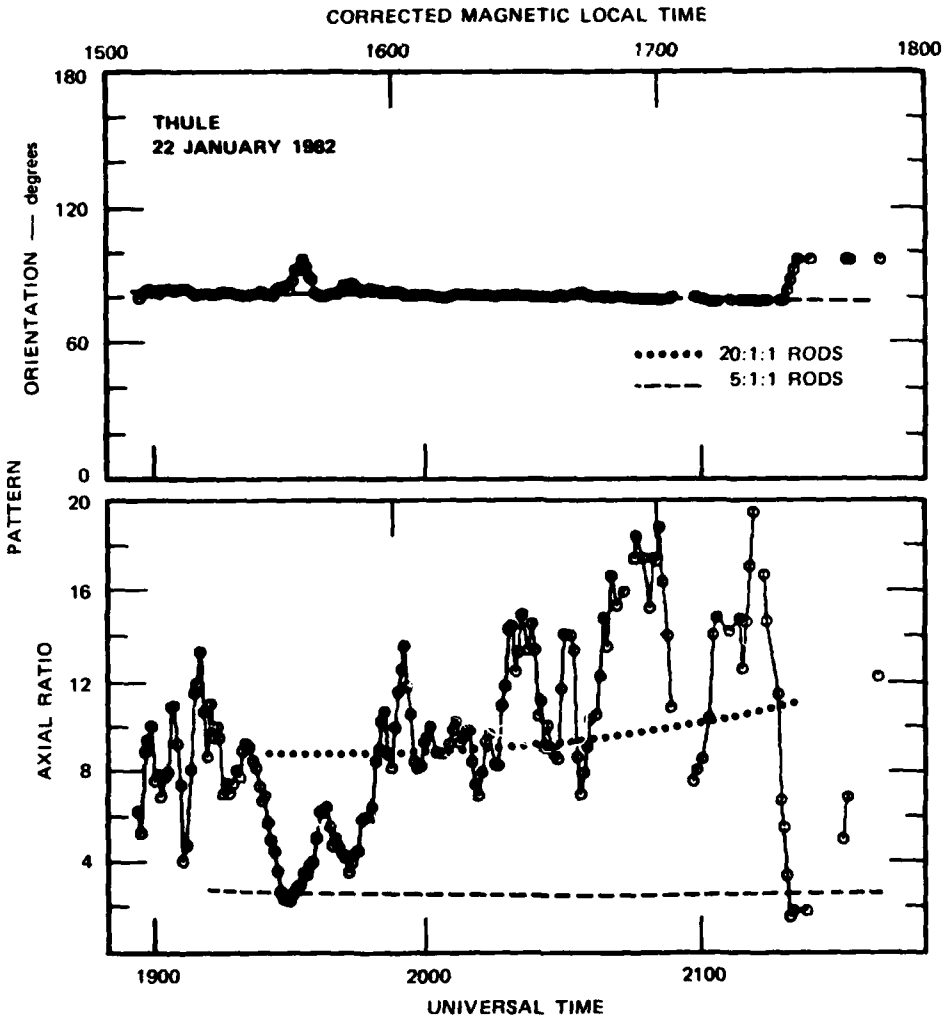

FIGURE 24 LOCAL-DUSK-SECTOR MEASURED AND MODEL PATTERN ANISOTROPY

A third set of data taken near local dusk on the same day is shown in Figures 24 and 25. The penetration latitude in this case is 86°, slightly northward of the other time-sector data. The irregularities are still rodlike, systematically increasing from about 20:1:1 elongation in mid-afternoon to about 40:1:1 by 2100 UT. This increase is associated with a general decrease in drift speed, although there is no clear association, feature-for-feature with the northward or eastward components. The northeastward drift in this case also fits the skewed two-cell flow pattern suggested by the dawn- and noon-sector data.

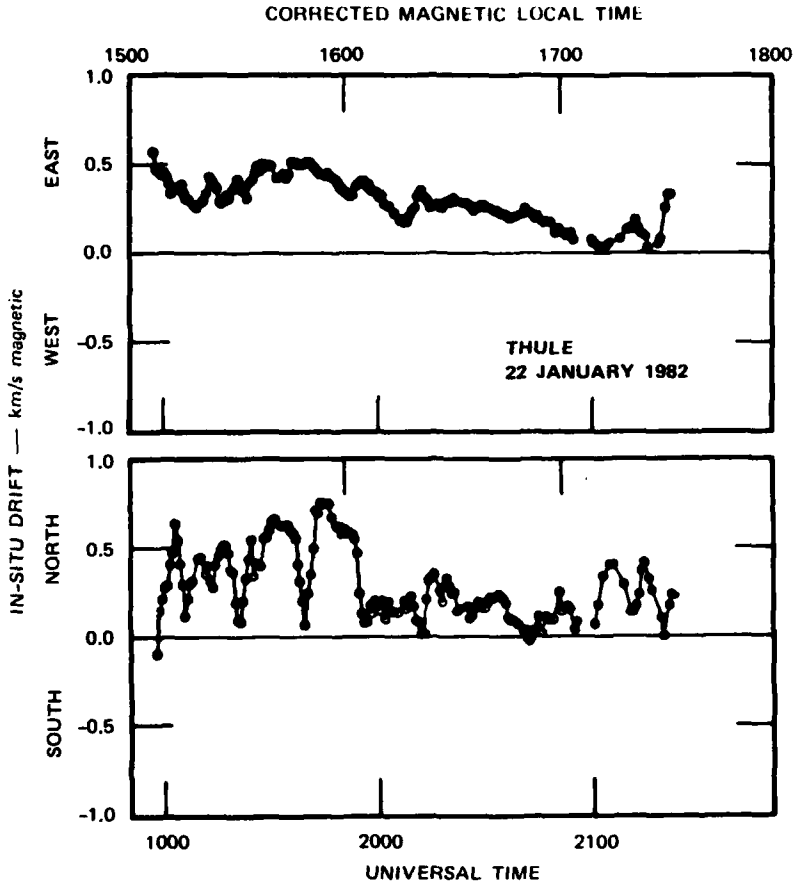

FIGURE 25 LOCAL-DUSK-SECTOR MEASURED IRREGULARITY DRIFTS

Detailed comparisons between these data and simultaneous ionosonde and optical observations are underway. Associations between particular anisotropy and drift features, and the large-scale polar-cap structures can then be established and the process of identifying instability processes can be initiated. From these measurements alone, however, we can make some preliminary conclusions appropriate to the DFA problem:

(1) The irregularities in the $\sim$ 600 m spatial wavelength regime are almost exclusively rodlike and range in extension from about 5:1:1 to 50:1:1. We note that on the day following our examples here, deviations from the rodlike structures do occur corresponding

to unusual drift flow patterns. For either irregularity type, scintillation levels for field-aligned propagation can be greatly and consistently enhanced. For the polar cap this will be at a near-vertical geometry.

(2) The measured drift patterns in the central polar cap fit the expected two-celled pattern and can exceed 800 m/s in the dawn, noon, and dusk sectors.

(3) An association exists between drift magnitude and direction, and irregularity anisotropy.

Convection dominance of anisotropy has been clearly demonstrated in the auroral zone, and presumably a similar process is ongoing in the polar cap. The large-scale dynamics of high-latitude fields are relatively well understood and are effectively modeled. As pointed out in Section B, if the anisotropy/drift associations can be defined, it will greatly simplify the global prediction of irregularity occurrence and DFA performance.

4. Polar-Cap Turbulence Strength

Soon after the initial polar beacon observations from Thule in late 1979, it was clear that the turbulence levels were routinely exceeding those simultaneously observed in the auroral zone. To illustrate that difference here, and to provide direct estimates of DFA beam distortion in the polar cap, turbulence levels for the noon sector on Day 22 have been calculated for use with the anisotropy and drift data in Figures 22 and 23.

The measured intensity scintillation index and calculated C_s levels are shown in Figure 26. The S_4 index and C_s trends are generally well correlated, although C_s exhibits a wider dynamic range than the S_4 index, which is saturated much of the time. The peak C_s levels here are near 10^{21}, significantly stronger than those observed in the auroral zone, but still weaker than peak values seen at the equator [Livingston et al., 1981].

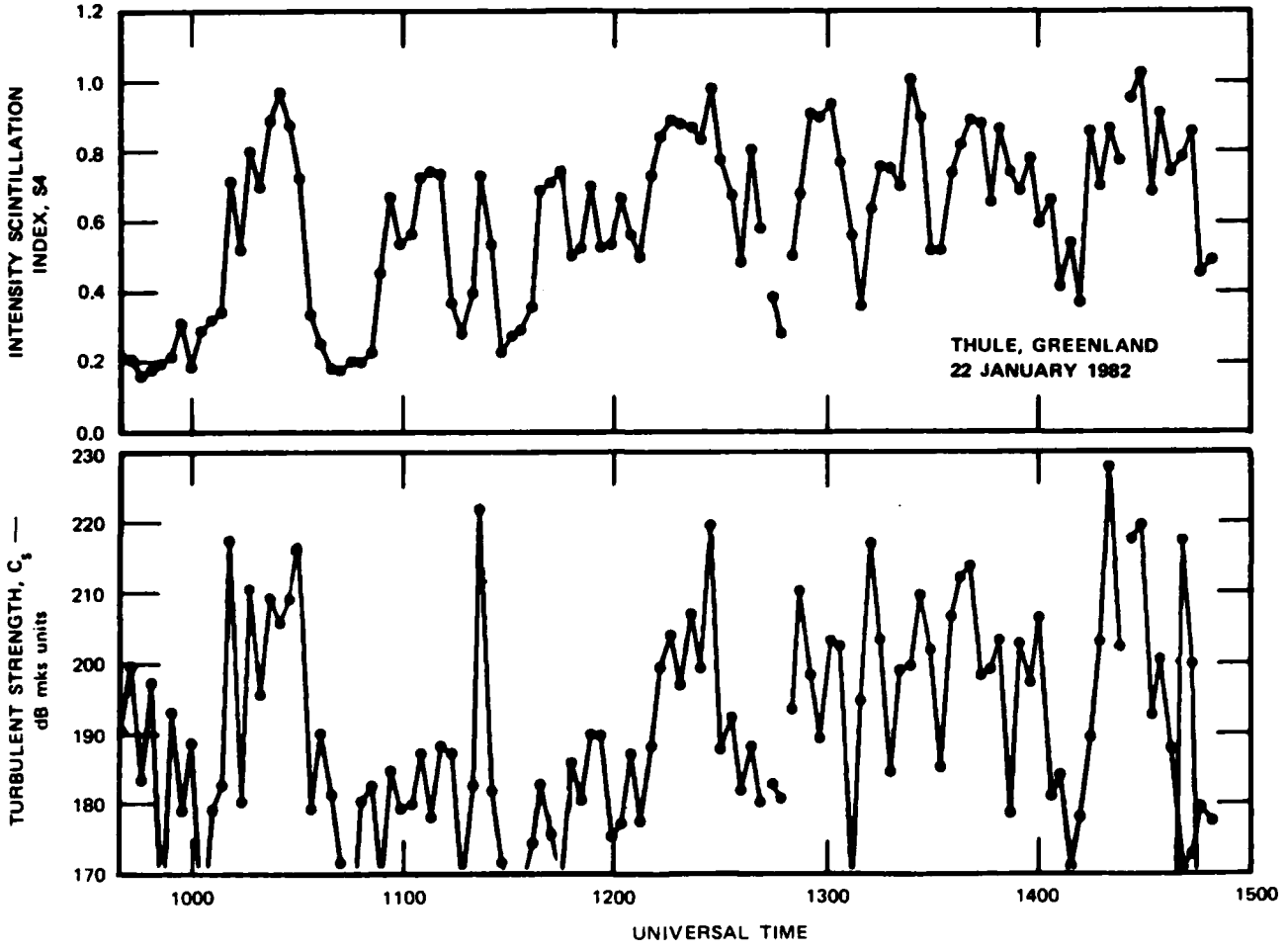

FIGURE 26 MEASURED INTENSITY SCINTILLATION INDEX AND ESTIMATED THREE-DIMENSIONAL TURBULENCE STRENGTH

We again consider two propagation situations, and the corresponding 1/e spatial correlation contours are shown in Figure 27. The first of these is for the average 20:1:1 measured axial ratio and observation geometry. The correlation surface in this case is highly anisotropic, with a minimum 1/e width of about 200 m at 244 MHz. At 1000 MHz, the pattern would be of similar shape, but wider. The second case in Figure 27 is for field-aligned propagation and more extended (50:1:1) irregularities. At 244 MHz, the degradation of performance would be significant even for small DFA apertures. For the 1000 MHz case shown, the decorrelation scale is about 200 m, much shorter than that in the auroral zone, but still not a severe constraint on moderate size DFA systems.

The scaling of the contours in Figure 27 for different C_s levels is similar to that for the auroral data, i.e., a 10-dB increase in C_s will roughly halve the decorrelation scale. The irregularities sampled for this data set are produced in the polar cusp and have drifted

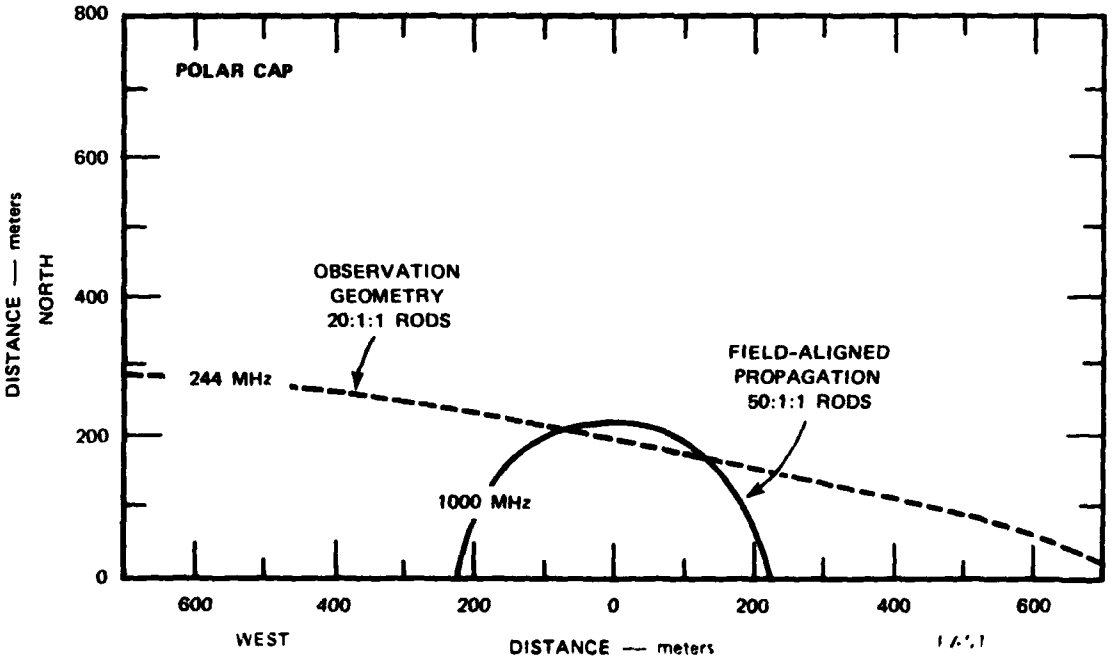

FIGURE 27 PREDICTED-SPATIAL-DECORRELATION PATTERN

into the central polar cap. In the polar cusp itself, turbulent levels will undoubtedly exceed the $C_s = 10^{21}$-dB level assumed here, and may be comparable to the $C_s > 10^{23}$-dB levels observed at the equator. Decorrelation scales less than 100 m could result, making the cusp a problem region for even moderate-sized apertures. Clearly, observations such as those discussed here should be made directly in the polar-cusp region.

VI SUMMARY AND DISCUSSION

In this report, we have identified the principal scintillation parameters that affect the performance of discrete focused arrays. We then reviewed recently-analyzed auroral-zone and polar-cap scintillation data to determine the potential for DFA performance degradation in those regions. We showed that the equivalent isotropic turbulence strength C_s, together with the power-law index parameter, sets the level of the perturbation. The irregularity anisotropy and the propagation geometry dictate the final degradation of the DFA performance.

For a nonadaptive system, the time structure of the scintillation affects only the detectability of the target. In an adaptive system, the spatial characteristics are varied in response to the current signal inputs. In that case, the time structure of the scintillation is important, but we have not addressed adaptive systems in this report.

In Sections V-B-2. and V-B-4. we show that moderate to severe propagation disturbances correspond to equivalent turbulence levels over a 100-km layer of 10^{20} and 10^{21} respectively. Figures 19 and 27 show the two-dimensional spatial-coherence structure. To determine the resultant degradation of DFA performance, we have used Equation (17) for a linear DFA aligned along the axis of maximum spatial coherence reduction. For a uniformly weighted array,

$$\langle |V_R(m\Delta K)|^2 \rangle = N \sum_{n=-(N-1)}^{N-1} 1 - \left|\frac{n}{N}\right| \exp\left\{-\tfrac{1}{2}C_{\delta\phi}^2 |n\delta\ell|^{p-1}\right\} \exp 2\pi\iota\frac{nM}{N} \qquad (39)$$

where $\Delta\ell\Delta K = 2\pi/N$. If $C_{\delta\phi}^2 = 0$, Eq. (39) reduces to Eq. (16).

Figure 28 shows the pattern degradation of a 16-element array with $\Delta\ell$ = 10 m. To calibrate the spatial wave-number scale, consider that the nulls occur at multiples of $\pi/N\Delta\ell$. The propagation effects broaden

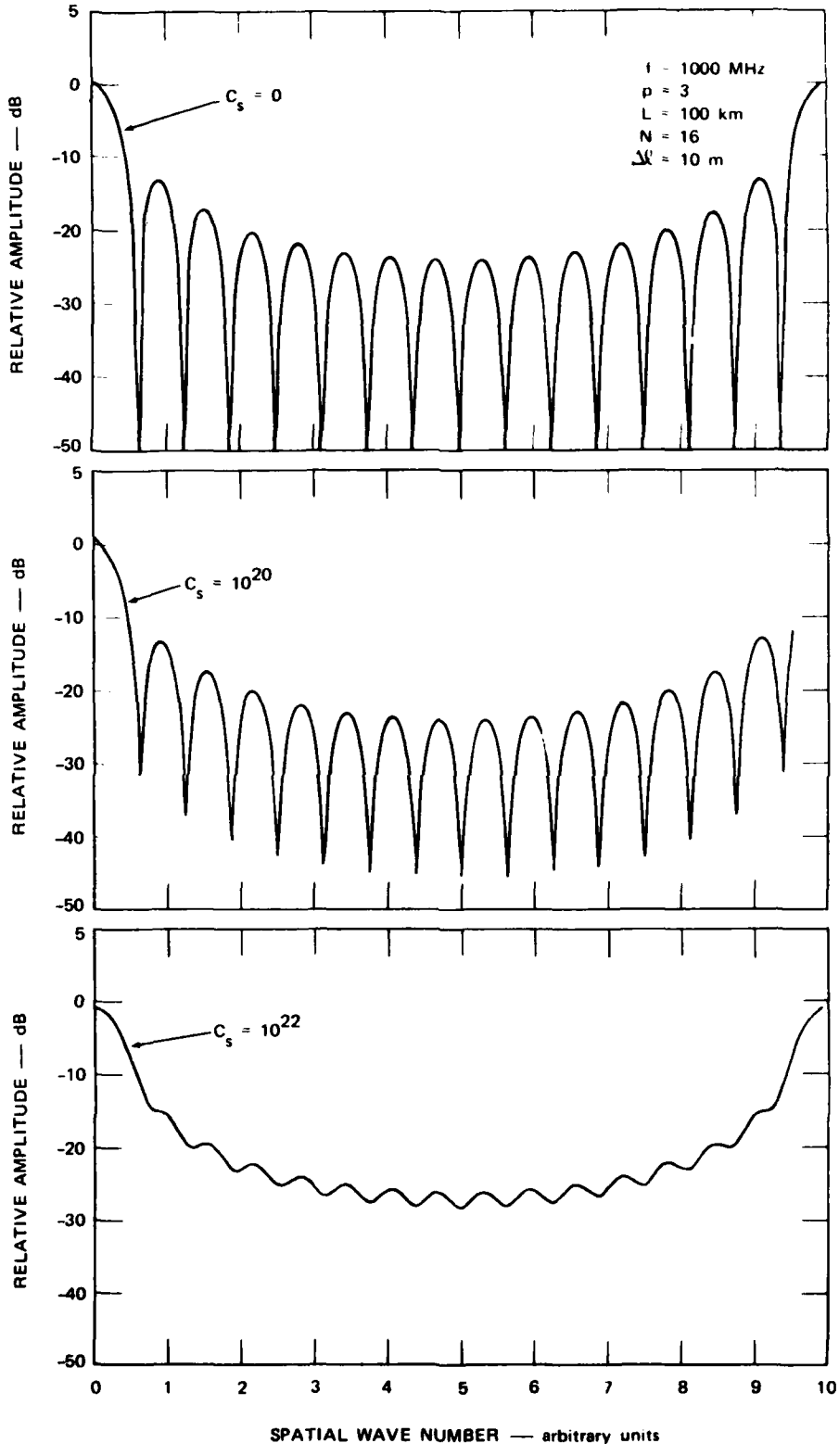

FIGURE 28 DEGRADATION OF LINEAR DFA PATTERN

the main beam and reduce the depth of the nulls. This is the average degradation, however, and individual realizations will show significant variations. In any case, severe performance degradation would be expected for the moderate-to-severe perturbation levels.

The current state of scintillation modeling and the available data base does not permit the actual probability of occurrence of severe DFA performance degradation to be specified. We do know, however, that severely disturbed regions are confined in latitude and strongly affected by convection and a conducting E-layer. The rudimentary elements of a global structure model have been described by Kelley et al. [1982]. The planned DNA HILAT satellite experiment should provide the necessary data base for implementing such a model.

We also note that a single power-law model does not accurately reflect the in situ irregularity structure; rather, the spectrum has a two-component structure with shallowly sloped and steeply sloped regiments separated at a wave=number corresponding to scale sizes between 500 m and 1 km [Rino et al., 1981; Kelley et al., 1982; Basu et al., 1982]. Accommodating the two-component structure does not affect the spatial coherence measures significantly, however, and the single component model can be used effectively for deriving DFA system performance measures.

We suspect that an understanding of the detailed spectral characteristics will ultimately improve our ability to predict the occurrence and lifetime of structure. Significant improvements in our predictive capability must await such refinements.

REFERENCES

Aarons, J., J. P. Mullen, H. E. Whitney, A. L. Johnson, and E. J. Weber, "UHF Scintillation Activity Over Polar Latitudes," Geophys. Res. Lett., Vol. 8, p. 277 (1981).

Armstrong, J. W. and W. A. Coles, "Analysis of Three Station Interplanetary Scintillation," J. Geophys. Res., Vol. 77, p. 4602 (1972).

Basu, S., S. Basu, R. C. Livingston, H. E. Whitney and E. Mackenzie, "Comparison of Ionospheric Scintillation Statistics from the North Atlantic and Alaskan Sectors of the Auroral Oval Using the Wideband Satellite," Air Force Geophysics Laboratory, AFGL Report AFCL-TR-81-0266 (1981).

Basu, S., S. Basu, J. P. McClure, W. B. Hanson, and H. E. Whitney, "High Resolution Topside in-situ Data of Electron Densities and VHF/GHz Scintillations in the Equatorial Region," in press, J. Geophys. Res. (1982).

Burke, W. J., M. C. Kelley, R. C. Sagalyn, M. Smiddy, and S. T. Lai, "Polar-Cap Electric-Field Structures with a Northward Interplanetary Magnetic Field," Geophys. Res. Lett., Vol. 6, p. 21 (1979).

Elachi, C., and D. D. Evans, "Effects of Random Phase Changes on the Formantion of Synthetic Aperture Radar Imagery," IEEE Trans. Antennas Propagat., AP-25, p. 149 (1977).

Fremouw, E. J., R. L. Leadabrand, R. C. Livingston, M. D. Cousins, C. L. Rino, B. C. Fair, and R. A. Long, "Early Results from the DNA Wideband Satellite Experiment--Complex Signal Scintillation," Radio Sci., Vol. 13, p. 167 (1978).

Fremouw, E. J., and J. M. Lansinger, "Recent High Latitude Improvement in a Computer Based Scintillation Model," Proceedings of Ionospheric Effects Symposium, Alexandria, VA (1981).

Friis-Christensen, E., K. Lassen, J. Wilhjelm, J. M. Wilcox, W. Gonzalez, and D. S. Colburn, "Critical Component of the Interplanetary Magnetic Field Responsible for Large Geomagnetic Effect in the Polar Cap," J. Geophys. Res., Vol. 77, p. 3371 (1972).

Heelis, R. A., W. B. Hanson, C. R. Lippincott, D. R. Zuccaro, L. H. Harmon, B. J. Holt, J. E. Doherty and R. A. Power, "The Ion Drift Meter for Dynamics Explorer-B," Space Sci. Inst., Vol. 5, p. 511 (1981).

Heppner, J. P., "The Harang Discontinuity in Auroral-Belt Ionospheric Currents," Geophys. Publ., Vol. 29, p.105 (1972).

Jordan, R. L., "The SEASAT--A Synthetic Aperture Radar System," IEEE J. Ocean. Engr., Vol. OB-5, p. 154 (1980).

Kelley, M. C., R. Pfaff, K. D. Baker, J. C. Ulwick, R. Livingston, C. Rino and R. Tsunoda, "Simultaneous Rocket Probe and Radar Measurements of Equatorial Spread-F--Transitional and Short Wavelength Results," J. Geophys. Res., Vol. 87, p. 1757 (1982).

Klobuchar, J., "Ionospheric Propagation Considerations for the NAVSTAR-Global Positioning System," Technical Memorandum No. 56, Air Force Geophysics Laboratory, Bedford, MA (1981).

Livingston, R. C., C. L. Rino, J. Owen, and R. T. Tsunoda, "The Anisotropy of High-Latitude Nighttime F-Region Irregularities," J. Geophys. Res., Vol. 87, No. A12, p. 10,519 (1982).

Livingston, R. C. C. L. Rino, J. Owen, and R. T. Tsunoda, "The Anisotropy of High-Latitude Nighttime F-Region Irregularities," J. Geophys. Res., Vol. 87, No. A12, p. 10,519 (1982).

Martin, E. and J. Aarons, "F-Layer Scintillations and the Aurora," J. Geophys. Res., Vol. 82, p. 2717 (1977).

Moorcroft, D. R. and K. S. Arima, "The Shape of the F-Region Irregularities, Which Produce Satellite Scintillations--Evidence for Axial Symmetry," J. Atmos. Terr. Phys., Vol. 34, p. 437 (1972).

Mozer, F. S. and R. Serlin, "Magnetospheric Electric-Field Measurements with Balloons," J. Geophys. Res., Vol. 74, p. 4739 (1969).

Rino, C. L., "Propagation Effects in Space-Based Surveillance Systems," SRI International Topical Report 1, DNA Contract DNA001-81-C-0010, SRI Project 2394, SRI International, Menlo Park, CA (1982a).

Rino, C. L., "On the Application of Phase Screen Models to the Interpretation of Ionospheric Scintillation Data," Radio Sci., Vol. 17, p. 855 (1982b).

Rino, C. L. and E. J. Fremouw, "The Angle Dependence of Singly Scattered Wavefields," J. Atmos. Terr. Phys., Vol. 39, p. 859 (1977).

Rino, C. L. and S. J. Matthews, "On the Morphology of Auroral Zone Radio-Wave Scintillation," J. Geophys. Res., Vol. 85, p. 4139 (1980).

Rino, C. L. and R. C. Livingston, "On the Analysis and Interpretation of Spaced-Receiver Measurements of Transionospheric Radio Waves," Radio Sci., Vol. 17, p. 845 (1982).

Rino, C. L. and J. F. Vickrey, "Recent Results in Auroral-Zone Scintillation Studies," J. Atmos. Terr. Phys., Vol. 44, No. 10, p. 875 (1982).

Rino, C. L., R. C. Livingston, and S. J. Matthews, "Evidence for Sheet-Like Auroral Ionospheric Irregularities," Geophys. Res. Lett., Vol. 5, p. 1034 (1978).

Rino, C. L., J. Petriceks, R. C. Livingston and C. H. Dawson, "Data Reduction and Analysis of Coherent Satellite Transmissions," Final Report, Contract 211-275012-40472, SRI Project 6449, SRI International, Menlo Park, CA (1977).

Rino, C. L., R. T. Tsunoda, J. Petriceks, R. C. Livingston, M. C. Kelley and K. D. Baker, "Simultaneous Rocket-borne Beacon and in-situ Measurements of Equatorial Spread-F--Intermediate Wavelength Results," J. Geophys. Res., Vol. 86, p. 2411 (1981).

Tsunoda, R. T. and J. F. Vickrey, "Evidence of East-West Structure in Large-Scale F-Region Plasma Enhancements in the Auroral Zone," accepted for publication, J. Geophys. Res., 1983.

Weber, E. J. and J. Buchar, "Polar-Cap F-Layer Auroras," Geophys. Res. Lett., Vol. 8, p. 125 (1981).